Acoustic Cavitation in a Microchannel

Siew-Wan Ohl and Claus-Dieter Ohl

Contents

Abstract

Cavitation in confined geometries, such as microfluidic channels, allows an unprecedentedly detailed look on their dynamics with a much better control as compared to cavitation in the bulk. Another advantage is that only small amounts

S.-W. Ohl
Institute of High Performance Computing, Singapore, Singapore

C.-D. Ohl (✉)
School of Physical and Mathematical Sciences, Nanyang Technological University, Singapore, Singapore
e-mail: cdohl@ntu.edu.sg

M. Ashokkumar (ed.), *Handbook of Ultrasonics and Sonochemistry*,
DOI 10.1007/978-981-287-278-4_6

of fluids are required. In these geometries, single or a few laser-generated bubbles are utilized for fundamental liquid processing such as mixing, sorting, and pumping. For acoustic cavitation, the bubbles need to be either injected a priori or generated through an entrainment process. Then cavitation can be utilized for emulsions, to lyse cells, to generate light (sonoluminescence), and to initiate chemical reactions. This review presents a summary of the effects of confinement on the bubble dynamics and how they can be utilized for research and applications.

Keywords
Cavitation bubbles • Microfluidic • Ultrasound • Cell

Introduction

It is difficult to observe a completely spherical and symmetric cavitation bubble collapse. The cavitation bubble collapse is influenced by the hydrostatic pressure gradient, imperfection in the bubble generation process, and the wall of the liquid container; all of them induce some asymmetry. These factors cause instabilities to develop during the collapse phase. It is well known that when a bubble collapses near a rigid structure, a high-speed liquid jet directed toward the structure is generated. During its collapse phase, the initially spherical bubble moves toward the structure and becomes toroidal with a thin jet in the center which attends a high velocity up to about 100 m/s [1, 2]. In a confined geometry such as a microfluidic channel, influences from the walls are expectedly more pronounced.

Although single-bubble dynamics is well studied, in many practical applications, a large number of cavitation bubbles need to be generated and controlled. This can be achieved through the use of a strong acoustic field. In section "How to Generate Cavitation?," we will show the method to generate strongly oscillating bubbles in a microfluidic channel. Two technical "tricks" have been used to overcome the constraints, namely, the lack of gas nuclei in the small liquid volume and the issue of transport of acoustic energy into the channel.

In section "Effects of the Microchannel on the Bubble Dynamics," the effect of confinement is discussed. Previous theoretical and experimental works are reviewed. Then the interaction of the bubble with a nearby object (such as a bubble, a cell, or a droplet) is described. The section ends with detailed review of several fundamental controls of microfluidic flow. Various mechanics such as pumping, switching, and sorting in microfluidics are examined.

The last section is devoted to applications involving acoustic cavitation and microfluidics. These include physical applications such as emulsification and chemical processes such as sonoluminescence and sonochemistry. We will also present some biomedical-related use of acoustic cavitation on a chip.

How To Generate Cavitation?

Generation of Single Cavitation Bubbles in Microfluidics

Cavitation bubble dynamics in all aspects have been studied in great detail. They have been summarized in a number of textbooks and comprehensive review articles. For readers seeking an introduction, we recommend the review article by Lauterborn and Kurz [3]. In that article, most of the knowledge for bubble dynamics in large fluid volumes is covered. Our focus in this chapter is on the dynamics of bubbles confined by two and more walls.

Cavitation bubble may be generated from bubbles that are already in the liquid, from gas pockets that are entrained or added to the liquid, or by nucleation. There are several bubble nucleation techniques. These include deposition of energy, for example, through an intense laser beam, or by stretching the liquid, that is applying a negative pressure. A stable gas bubble can be converted into a cavitation bubble by expanding the bubble to about twice its original size [4]. This can be achieved by a short exposure of the bubble to a low-pressure field in which the bubble expands or by resonant excitation. Both methods of bubble nucleation work in confined geometries too. A venturi nozzle reduces the pressure of the liquid easily below the vapor pressure. Mishra and Peles [5] report on such kind of devices and their observation of the resulting cavitating flows. The pressure can also be reduced by evaporation of liquid with a pinned liquid meniscus. Evaporation causes the liquid droplet to pin to the solid surface by maintaining its surface area but reducing its contact angle. The liquid meniscus is therefore said to be pinned to the interface. Subsequently the droplet will shrink. Cavitation bubbles generated by pressure reduction from liquid droplet evaporation can be found in nanochannels [6], in synthetic trees [7], or in droplets trapped in drying hydrogels [8].

Resonant excitation of gas bubbles and their transformation can be achieved by irradiating the liquid in the microchannel with ultrasound. Many different approaches to achieve sufficient pressure inside the fluidic channel have been reported in literature. We are to highlight a few out of the long list. A straightforward approach is to use a sonicator and adapt it to a microfluidic channel [9]. A more integrated approach was developed by Tandiono et al. [10, 11] by attaching a piezoelectric transducer to the glass substrate that supports the microfluidic channels. In this design, the acoustic field serves two purposes; firstly, the sound field generates Faraday waves [12], which entrain bubbles into the liquid in the microfluidic channels. These bubbles then start to oscillate, resonantly, and create intense cavitation. Further discussion on acoustic bubbles is given in the following section.

Another method of generating cavitation bubbles in microfluidics is by energy deposition (Fig. 1). The laser source is a Nd:YAG laser and some part of the laser beam is utilized through an optical delay for illumination. Experimental results from single and multiple bubbles generated with a laser are presented in the next section.

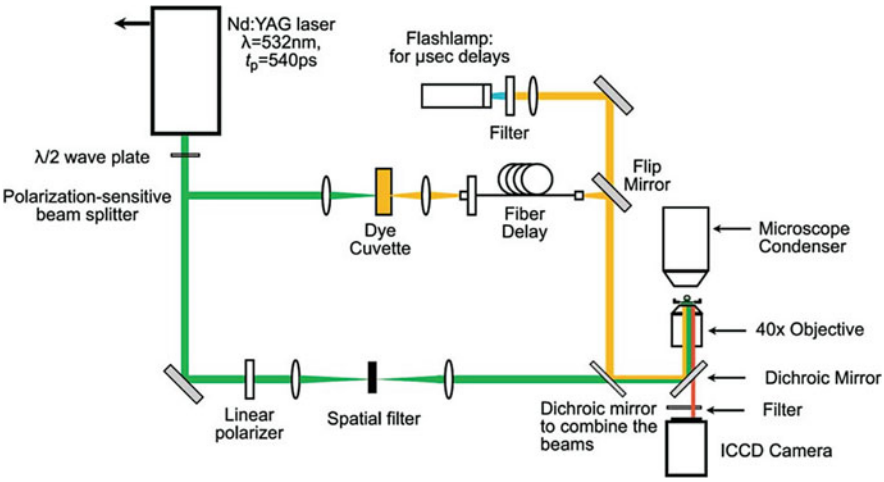

Fig. 1 Experiment setup for time-resolved fluorescence imaging

Before we come to the details, we want to highlight that several approaches have been utilized to create laser-induced bubbles in microfluidics: by linear absorption, by multiphoton absorption, and by plasmonic absorption. Linear absorption utilizes a liquid containing a dye with a high absorption coefficient at the laser wavelength [13]. This allows fine adjustment of the bubble size through the laser energy manipulation. The downside is that objects in the liquid may come into contact with the dye. This interaction is undesirable especially for biological cells. Nonlinear absorption [14] allows bubbles to be created in otherwise transparent liquids. However, the absorption process possesses a threshold, and therefore only relatively large bubbles can be generated. Plasmonic absorption can be achieved by deposition of a thin gold layer on the substrate. A green laser is then targeted to the gold layer for bubble nucleation. This approach is particularly attractive for studies with cells [15].

Acoustic Cavitation in Microfluidics

The bubbles used in microfluidics for mixing and pumping are often oscillating only gently. They are introduced either by direct injection [16] or trapped gas [17]. It is difficult to create cavitation bubbles in microfluidics by acoustics. Two main hurdles that have to be overcome are the lack of nucleation sites and the difficulty in transmitting high-pressure amplitude ultrasound into the microfluidic channels. The small volume of fluid in the microfluidic channels does not contain many pre-existing gas pockets or impurities which act as nucleation site of the cavitation bubbles. It is not practical to put an ultrasound transducer inside the microfluidic channels. Often the ultrasound is generated externally by transducers attached to the glass plate onto which the microfluidic channels are attached [10, 18]. The fragility

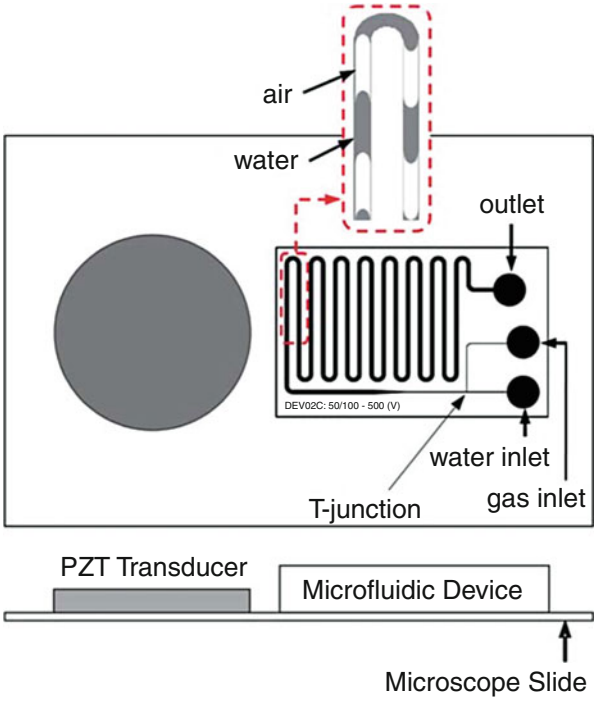

Fig. 2 The design and setup of the microfluidics device for the generation of intense cavitation. The transducer generating ultrasound is attached on the left side the microfluidic channel which is made of polydimethylsiloxane (PDMS) on a glass slide of 75×50 mm^2. The width of the T-junction is 50 μm and 100 μm for the gas and the main (water) channels, respectively. The main channel expands to 500 μm downstream. The height of the channel is 20 μm. The zoomed *inset* shows a typical configuration of the liquid–gas slugs in the channel (Reproduced with permission from Ref. [5], Fig. 1)

of the system (both the polydimethylsiloxane (PDMS) and the thin glass slide) prevents the use of high-intensity or large transducers.

Iida et al. [18] investigated the use of mild ultrasound (about 0.5 MPa) to generate cavitation bubble in a millimeter-sized channel or chamber. They used an external transducer which is attached to the bottom of their devices. They compare the results from these 1D channel and 2D chamber to that of a 3D (20 millimeter in height) glass tube. They measured the production of cavitation bubbles indirectly by monitoring the generation of fluorescent hydroxyterephthalate (HPTA) from the chemical reaction between terephthalate anion with OH radicals which are produced by ultrasonic cavitation. Higher ultrasonic power is needed to generate HPTA in the channel and chamber as compared to the tube.

Tandiono et al. [10] reported the first successful attempt to generate intense acoustic cavitation in a microfluidic channel. They overcome the problems mentioned by having a gas inlet (see Fig. 2). The gas pockets in the fluid form a large number of gas–liquid interfaces. The gas–liquid boundaries become the nucleation sites of the acoustic cavitation. On the same glass slide as the microfluidic channel, coin-shaped ultrasound transducers are attached. The ultrasound waves cause the gas–liquid interface to oscillate. At high-oscillation amplitude, these surface waves entrap gas pockets which expand and oscillate (see Fig. 3). The acoustic cavitation bubbles thus generated are used to create sonoluminescence and sonochemistry [11], cell disruptions or stretching [19, 20], and emulsification [21]. Details of these applications are given in the subsequent sections.

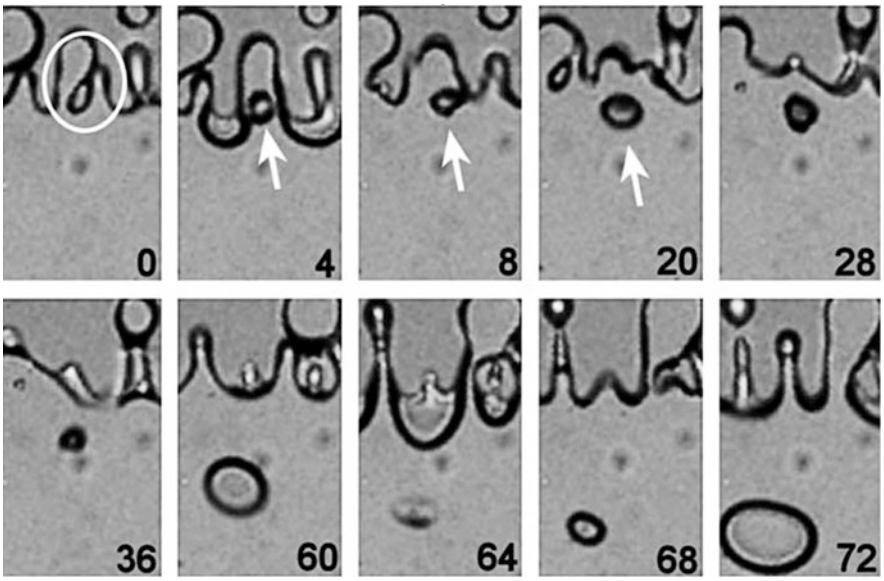

Fig. 3 The entrapment of gas pocket in a microfluidic channel. The air is on *top* and the water *below*. The number in each frame indicates the time in microsecond, and the frame width is 100 μm. The transducer is driven at 50 V, 100 kHz. In the first frame, the crest is *circled*. In the second, third, and fourth frames, the *arrows* point to the location where a gas nucleus is formed. The ultrasound causes this gas pocket to oscillate in the subsequent frames (Reproduced with permission from Ref. [5], Fig. 4)

Ultrasound Contrast Agents

Apart from cavitation bubbles, there is another type of bubble which is either generated in microfluidics or used in microfluidic research. It is known as the ultrasound contrast agent (UCA). These bubbles are typically in micron size (about 1–3 μm in radius). They are stable bubbles because of a lipid or polymer coating on the bubble surface. The bubble core is made of air or heavy gases such as perfluorocarbon.

The UCAs are used in ultrasound imaging for contrast enhancement [22]. They are injected intravenously into the blood circulation system. The bubbles oscillate and reflect the ultrasound. The echo generated allows the differentiation between the blood vessels and the surrounding tissues resulting in clear ultrasound images. Without the UCA bubbles, the echogenicity difference between the blood and its surrounding tissues is not strong.

Experiments with Ultrasound Contrast Agents (UCAs)

Experiments on UCA concentrate on the delivery of drug or gene into targeted tissue or cells. The loading of the drug or gene is performed in multiple ways. The drugs could be loaded on the surface of the microbubbles by ligands [23, 24]. The ligands

bind the drug molecules and the lipid layer on the bubble. Alternatively, the drug is dissolved in an oil layer within the microbubble [23]. In some cases, especially for gene transfection, the genetic material (e.g., plasmid DNA) is incorporated within the lipid layer [24].

After being injected into the bloodstream, the delivery of drug or gene is activated by ultrasound when the UCAs are detected by imaging to be near the targeted area (site of tumor, tissues to be transfected et cetera). The acoustic pressure waves cause the microbubbles to oscillate or collapse. The drug or gene is then dispensed from the bubbles to the surrounding tissues. Details of the mechanism of drug/gene delivery by UCA could be found in [24, 25].

These loaded UCAs have been studied to treat multiple illnesses and genetic disorders [23, 26, 27]. Since UCA has been developed initially for echocardiography, it is investigated for therapeutic treatment for the heart. Detail applications are presented and discussed in [23]. They include the use of UCA for sonothrombolysis and drug/gene delivery. Recent animal study from Wu et al. [28] suggests that the use of microbubbles (and ultrasound) and drug is a good treatment modality for heart attack (myocardial infarction). Datta et al. [26] present a systematic study of the use of ultrasound and microbubbles for the removal of blood clot. They find the ultrasonic bubbles enhance the removal of the blood clot and the delivery depth of the drug into the clot. While sonothrombolysis for heart and transcranial ultrasound surgery has been done for animal [28] and human trials [29], gene therapy is progressing at a slower pace. Successful tissue and animal trials have been reported [26, 30]. UCA gene delivery has the virtue of being nonviral and potentially noninvasive.

Effects of the Microchannel on the Bubble Dynamics

Single and Few Bubbles in Confined Environments

Cavitation bubbles in confined geometry have interesting properties to actuate and manipulate microfluidic fluid flow and the objects within the channels. These properties drive the research interest in this area. This chapter is organized by first introducing the simple models which describe the flow from single and multiple oscillating bubbles in a thin gap. We will then discuss the interaction of the bubbles with objects of interest before we address specific fluid flows created by single and few bubbles.

Modeling Approaches

We will first discuss a simplified approach to model bubbles by reducing the Navier–Stokes equation into an ordinary differential equation (ODE). Ignoring viscous and thermal effects, few-bubble systems can be described by a set of ODEs, including their transversal motion. However, particular qualities of the flow

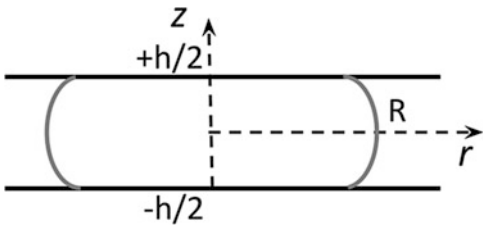

Fig. 4 Side view of a bubble with lateral radius R being constrained by two horizontal plates separated by a distance h

induced by the bubble cannot be described within above framework. Objects in the thin gap may undergo large shear. For this to occur, we need to account for the development of a nonuniform flow profile and, in particular, for the formation and separation of boundary layers. An example of the flow obtained from computational fluid mechanics is given resembling oscillatory flow in thin gaps.

Single-Bubble Ordinary Differential Equations

Next we derive a general ordinary differential equation describing the oscillation of a bubble in a thin gap with a planar flow following closely the derivation from Xiong et al. [31]. The radius of the cylinder is R and it is confined in a channel of height h. The geometry is sketched in Fig. 4.

We use an axisymmetric coordinate system (r, z, θ) and ignore translational motion of the bubble. Bubble motion will be discussed in section "Computational Fluid Dynamics (CFD) of Single Bubbles." The liquid is assumed incompressible; hence the fluid flow is given by the Navier–Stokes (NS) equation:

$$\frac{\partial u}{\partial t} + \left(\vec{u} \times \nabla\right) \vec{u} = -\frac{1}{\rho}\nabla p + \frac{\mu}{\rho}\nabla^2 \vec{u}, \tag{1}$$

where ρ is the density of the fluid, μ is the dynamic viscosity, $\vec{u}$ is the liquid velocity, and p is the pressure. As the problem is axisymmetric, i.e., $\partial/\partial\theta = 0$, planar flow depicts $u_z = 0$, and ignoring any swirl $u_\theta = 0$, we obtain the NS equation of the radial component:

$$\varrho\left(\frac{\partial u_r}{\partial t} + u_r\frac{\partial u_r}{\partial r}\right) = -\frac{\partial p}{\partial r} + \mu\left[\frac{1}{r}\frac{\partial}{\partial r}\left(r\frac{\partial u_r}{\partial r}\right) + \frac{\partial^2 u_r}{\partial z^2} - \frac{u_r}{r^2}\right] \tag{2}$$

As the continuity equation demands that $\nabla \cdot \vec{u} = 0$, one can show that the radial velocity component has the form $u_r = \frac{G(z,t)}{r}$, where G is an arbitrary function. Inserting this expression into Eq. 2, it simplifies into

$$\rho\left(\frac{\partial u_r}{\partial t} - \frac{u_r^2}{r}\right) = \frac{\partial p}{\partial r} + \mu\frac{\partial^2 u_r}{\partial z2} \tag{3}$$

Equation 3 can be integrated once across the channel height to obtain

$$\rho\left(\frac{\partial\overline{u_r}}{\partial t}-\frac{\overline{u_r^2}}{r}\right)=-\frac{\partial p}{\partial r}+\frac{2\tau_w}{h}, \tag{4}$$

where $\tau_w=\mu\frac{\partial u_r}{\partial z}$ is the shear stress at $z=\pm h/2$, i.e., at the channel walls. Conservation of mass with the boundary condition at $u_z(r=R)=\frac{dR}{dt}=\dot{R}$ demands that the averaged velocity is $\overline{u_r}=R\dot{R}/r$. Inserting this expression into Eq. 4, we obtain an ordinary differential equation in R:

$$\frac{\rho}{r}\left(R\ddot{R}+\dot{R}^2\right)-\frac{\rho}{r^3}R^2\dot{R}^2=\frac{\partial p}{\partial r}+\frac{2\tau_w}{h}. \tag{5}$$

We now integrate Eq. 5 from R_∞ to R in the radial direction resulting into

$$\left(R\ddot{R}+\dot{R}^2\right)\ln\frac{R}{R_\infty}+\frac{\dot{R}^2}{2}\left(1-\frac{R^2}{R^2{}_\infty}\right)=\frac{p(R_\infty)-p(R)}{\varrho}+\frac{2}{h\varrho}\int_{R_\infty}^{R}\tau_w dr, \tag{6}$$

where $p(R)$ is the pressure in the liquid at the bubble surface. The logarithmic singularity in the first term of Eq. 6 prevents to set integrate to infinity but only to a finite size R_∞ which is typically the dimension of the microfluidic container.

The wall shear stress is not specified in Eq. 6 and depends on the velocity profile $u_r(z)$. Next we assume a Poiseuille-type flow, thus a quadratic flow velocity profile with no-slip at the channel walls τ_w and insert into Eq. 6, thus

$$u_r=\frac{f(r,t)}{2\mu}\left(z^2-\frac{h^2}{4}\right). \tag{7}$$

Here the function $f(r, t)$ can be obtained from mass conservation. Therefore, Eq. 7 is integrated over the channel height and equated to the mass flux at the bubble wall:

$$2\pi Rh\dot{R}=2\pi rh\overline{u_r}=2\pi rh\left(-\frac{f(r,t)h^2}{12\mu}\right). \tag{8}$$

We can now solve Eq. 8 for the velocity $u_r(z)$, calculate the wall shear stress τ_w, and insert into Eq. 6:

$$\left(R\ddot{R}+\dot{R}^2+\frac{12\mu}{h^2\varrho}R\dot{R}\right)\ln\frac{R}{R_\infty}+\frac{\dot{R}^2}{2}\left(1-\frac{R^2}{R^2{}_\infty}\right)=\frac{p(R_\infty)-p(R)}{\varrho}. \tag{9}$$

Equation 9 is a Rayleigh–Plesset-type equation for a single bubble in a channel which accounts for viscous dissipation. We assume that the shape of the bubble does not change during the bubble oscillation; the bubble remains in a cylindrical shape with a constant contact angle Θ (liquid side). The pressure balance at the bubble wall

(ignoring normal viscous stresses) allows to relate the bubble pressure with the pressure in the liquid at the bubble wall:

$$p(R) = p_v + p_g - \Delta p = p_v + p_{g0}\left(\frac{R_0}{R}\right)^{3k} - \sigma\left(\frac{1}{R} + \frac{2\cos\Theta}{h}\right). \tag{10}$$

Here, p_v is the vapor pressure, p_g is the gas pressure, and Δp is the jump due to surface tension. The gas pressure p_g is related to the gas pressure at equilibrium p_{g0} through the bubble radius R_0 at equilibrium and the polytropic exponent κ assuming an ideal gas law. The coefficient of surface tension is σ and the Laplace pressure has contributions from two radii of curvature.

Depending on the geometry, Eqs. 9 and 10 can be simplified, e.g., for sufficiently large channel gaps h; the contribution from viscosity in Eq. 9 and surface tension Eq. 10 may be ignored. A comparison of the bubble dynamics in a $h = 8$ μm and a $h = 700$ nm thick channel is presented in Fig. 5 as solid lines. The dashed lines show the dynamics in absence of the viscous contribution, while the symbols present experimental measurements.

During the initial expansion of the bubble from a size smaller than the gap height, the liquid flow will be a mixture of a 3D spherical and a 2D planar flow. To account for this, Leighton [32] provides corrections to the inertia term, i.e., LHS of Eq. 6.

Multiple Bubble Ordinary Differential Equations

If more than one bubble is present, interaction of the bubbles needs to be taken into account. The interaction between bubbles can be derived straightforwardly assuming potential flow of two or more cylindrical bubbles. A convenient approach to derive the equations of motion for the radial and the translational motion is the Lagrange formalism [33–35]. The geometry for two interacting bubbles is sketched in Fig. 6, together with the arbitrary origin O, and the variables used in the equations below. A full derivation is stated in Quinto-Su et al. [36]. The resulting equations of motions are

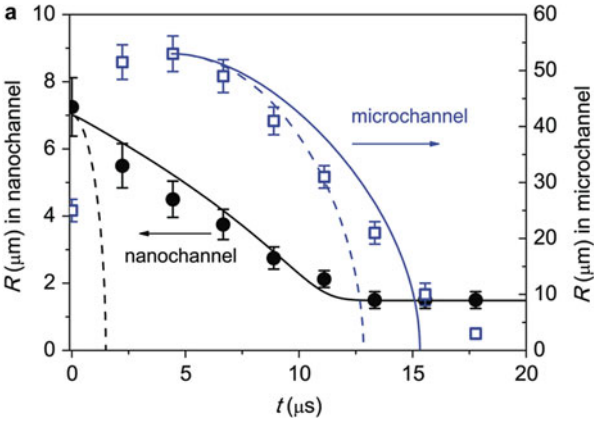

Fig. 5 (**a**) Comparing the radial dynamics of a bubble in the extended nanochannel with 8 μm (*hollow square*) with a viscid 2D model (*solid line*) and inviscid 2D model (*dashed line*). Left axis is for the bubble in extended nanochannel and the right one is for the bubble in a microchannel

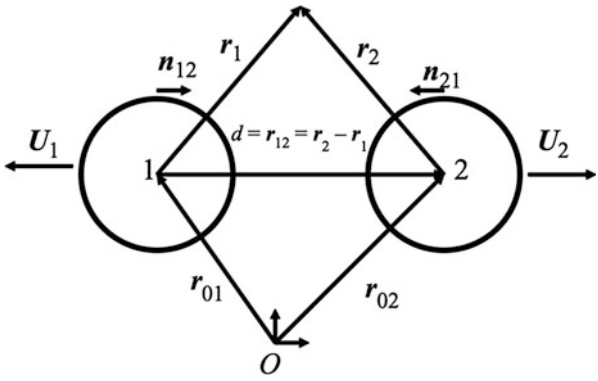

Fig. 6 Sketch of the bubble geometry and variables for bubble–bubble interaction. The positions of the bubbles 1 and 2 with radii R_1 and R_2 have their centers at $\boldsymbol{r_{01}}$ and $\boldsymbol{r_{02}}$ and translate with velocities $\boldsymbol{U_1}$ and $\boldsymbol{U_2}$ (Reproduced with permission from Ref. [36], Fig. 1)

$$\left(\ddot{R}_i R_i + \dot{R}_i^2\right)\log\left(\frac{R_i}{R_\infty}\right) + \frac{\dot{R}^2}{2} = \frac{p}{\varrho}\frac{-\vec{U}_i^2}{2} - \sum_{k\neq i}\left(\ddot{R}_k R_k + \dot{R}_k^2\right)\log\left(\frac{r_{ik}}{R_\infty}\right), \qquad (11a)$$

and

$$\ddot{\vec{r}}_{0i} = -\frac{2\dot{R}_i\,\vec{U}_i}{R_i} + \sum_{k\neq i}\frac{\vec{n}_{ki}(\ddot{R}_k R_k + \dot{R}_k^2)}{r_{ki}}. \qquad (11b)$$

The pressure p in Eq. 11a is the pressure difference between the pressure at infinity and the pressure in the bubble. Equation 11a is a modified cylindrical Rayleigh equation for bubble i with two additional pressure terms on the RHS: the first is caused by the bubble translation and resembles a stagnation pressure and the second term is pressure induced by the neighboring bubble.

The sum in Eq. 11a includes all bubbles, except bubble i. A comparison of this model with two cavitation bubbles recorded with a high-speed camera at 500,000 frames is shown in Fig. 7. The bubbles are created with two laser foci at a distance of 70 μm with a smaller bubble on the left and a larger on the right, Fig. 7a. Both the radial and the translational models are well described using only the initial radial velocity of the bubbles as a fit parameter. For this example the pressure p in Eq. 11a was taken as the ambient pressure as laser-induced bubbles in water contains mostly condensable gas; surface tension and normal viscous stresses are not relevant. Yet, for more viscous liquid or gas bubble oscillations, a restoring gas pressure must be taken into account similar to Eq. 10.

Computational Fluid Dynamics (CFD) of Single Bubbles

Oscillating bubbles in a narrow gaps may not form a parabolic flow profile instantaneously as assumed in Eq. 7. The timescale to develop a flow field is given by the diffusion of vorticity which is of the order of $\Delta t = \rho l^2/\mu$, where l is a length scale, e.g., $h/2$, for the above $h = 8$ μm channel $\Delta t = 16$ μs which is of the order of the bubble oscillations.

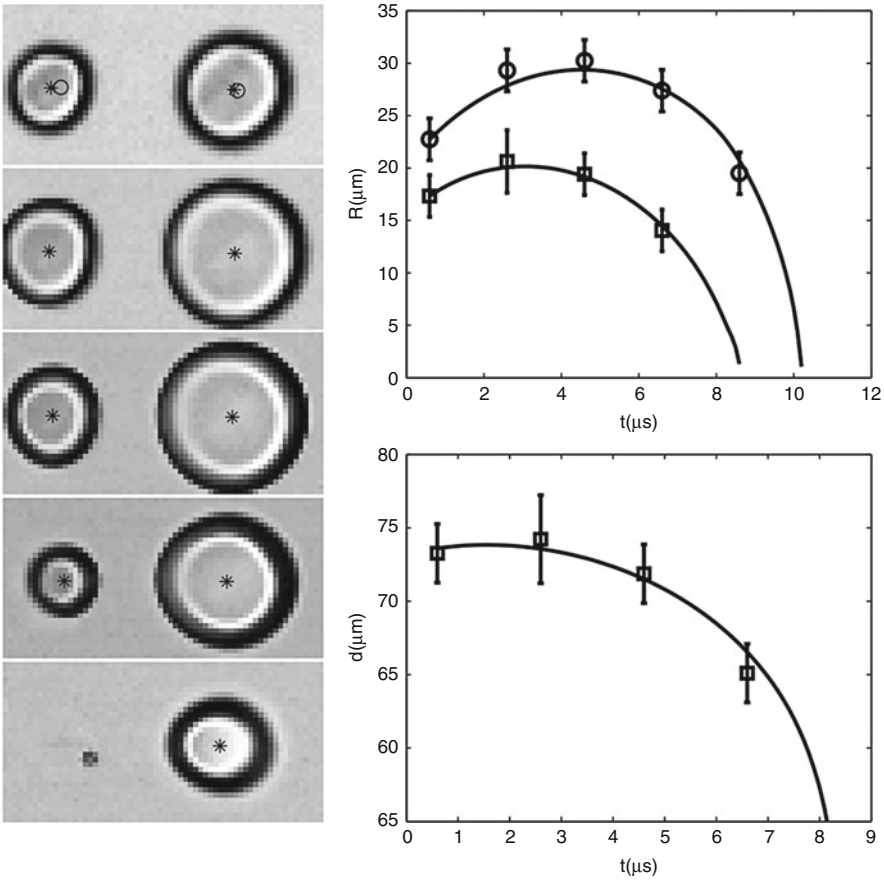

Fig. 7 Two unequal-sized bubbles created at a distance of 70 μm. The interval between two frames is 2 μs and the frame width is 128 μm. *Top right* figure denotes the radii in time for both bubbles. The *bottom right* figure shows the inter-bubble distance variation in time (Reproduced with permission from Ref. [36], Fig. 5)

We cannot therefore simply assume that the flow has developed. Additionally, during the initial expansion phase, the pressure inside the bubble might be higher than the surrounding fluid. During expansion, the pressure in the bubble drops, while the pressure far from the bubble might be higher, and an adverse pressure gradient builds up. The boundary layer may separate and give rise to a complex flow pattern with reverse flow, vorticity transport, and stagnation points inside the channel.

Axisymmetric radial flows of real fluids in narrow gaps have been studied experimentally and analytically in the past 50 years due to their relevance in industrial applications such as radial viscometers, radial diffusers, nonrotating air bearings, and disk-type heat exchangers, e.g., see Elkouh [37] and Von Kerczek [38] for analytical solutions to flows of a harmonically oscillating source at the center.

To demonstrate the importance of boundary layers, we present here a solution to the Navier–Stokes equation using the volume of fluid method with a level-set approach for the liquid–gas interface; for details see Li et al. [39]. The simulation starts with a pressurized spherical gas cavity in the center of a 20 μm high gap filled with a stagnant liquid (water).

Figure 8 depicts the temporal evolution of the bubble shape for 10 μs, thus an order of magnitude shorter than the vorticity diffusion time Δt. The spherical bubble quickly grows into a pancake shape, forming thin liquid films at the upper and lower solid walls. The maximum bubble radius is obtained after 4 μs. During bubble shrinkage, the convex interface flattens and only increases curvature after 8 μs, that is, when the internal pressure increases and dampens the collapse of the bubble. The bubble collapses to its minimum volume at $t = 10$ μs and rebounds afterward (not shown here). Right to the bubble profile in Fig. 8, the radial velocity profile at a distance of $r = 50$ μm from the bubble center is shown. Initially, the liquid is at rest and rapidly develops into a plug flow with strong wall shear stress. Gradually, a more parabolic profile develops. At the later expansion stage, the velocity near the walls is reduced and reversed in direction, while the liquid velocity in the center of the gap is still outward and positive. A more detailed study reveals that the adverse pressure gradient is responsible for the flow reversal.

Cavitation bubble dynamic modeling by solving the full Navier–Stokes equations in tubes has received more attention than in a planar gap. For example, Yuan and Prosperetti [40] and Ory et al. [41] have studied the pumping effect originating from vapor bubble expansion and collapse in tubes. Ye and Bull [42, 43] describe the therapeutical method of gas embolotherapy, where the expansion of liquid into a vapor shuts of nutrition supply to a malignant tumor. Their work [43] extends the

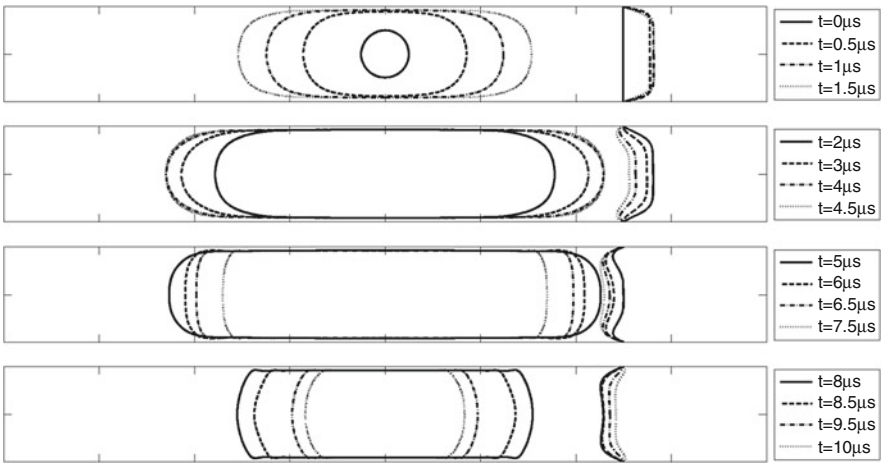

Fig. 8 Bubble shape evolution together with the radial liquid velocity profile at $r = 50$ μm from the center of the bubble. Please note the reversal of the flow direction near the boundaries occurring before the flow in the center of the gap

bubble oscillation into flexible tubes with the important finding that wall shear stress are greatly reduced once the constraining tube can elastically deform.

Effect of the Gap Height and Geometrical Shape on Bubble Dynamics

So far the bubble size considered is comparable and larger than the width of the gap, and the bubble center was located at the center of the gap. In many applications, bubbles are created close to one of the walls, e.g., on micro-heaters embedded in one of the plates. For narrow channels one can expect that the bubble fills quickly most of the gap. In contrast, if the gap is very large, the bubble is less affected and oscillates similarly to the situation where it is bounded by a single plate [44].

In a systematic study, Gonzales-Avila et al. [45] report about three scenarios and categorize them according to the nondimensional maximum bubble radius $\eta = h/R_x$, where h is the gap height and R_x the maximum bubble radius in the plate direction. Figure 9 depicts a collection showing that bubbles created in a very narrow gap expand and collapse by filling most of the channel, i.e., a disk-shaped bubble. For $0.4 < \eta < 1.0$, the bubble collapses onto the opposing side of the channel. The bubble migrates away from the plate it has been created. In the regime $1.0 < \eta < 1.4$, the bubble collapses mostly in the center of the channel, while for larger η-values, the collapse proceeds on the plate the bubble has been nucleated.

If the bubble is further constrained by lateral walls, complex jetting phenomena are observed. Zwaan et al. [46] showed that the bubbles can develop multiple jets. The number of jets corresponds to the number of nearby boundaries. Figure 10 depicts a bubble collapsing in a channel with two jets along the channel, three jets within an equilateral triangle, and four jets in a square chamber. The jets start from regions where there the largest volume of liquid is.

We have seen before that jets can be induced by a second nearby bubble which for a potential flow resembles a rigid boundary at half the distance between the bubbles. Another way to generate liquid jets is through an asymmetry of the bubble itself. This asymmetry can be conveniently generated with laser-induced bubbles, by either altering the shape of the focus or by creating multiple bubbles nearby which upon expansion coalesce and thereby form odd-shaped bubbles. An example for a toroidal bubble is shown in Fig. 11. There the laser focuses in on a circle resulting into to an annularly expanding bubble with a stagnation point in its center; see Lim et al. [47]. This specific laser focus was generated with a digital hologram and an objective lens acting as a Fourier lens.

Interaction of Single and Few Bubbles with Objects

Control over time and strength of the bubble dynamics enable the utilization of the bubble for manipulation of objects. In the paragraphs below, some of the work using cavitation bubble dynamics to study rheological properties of suspended objects are

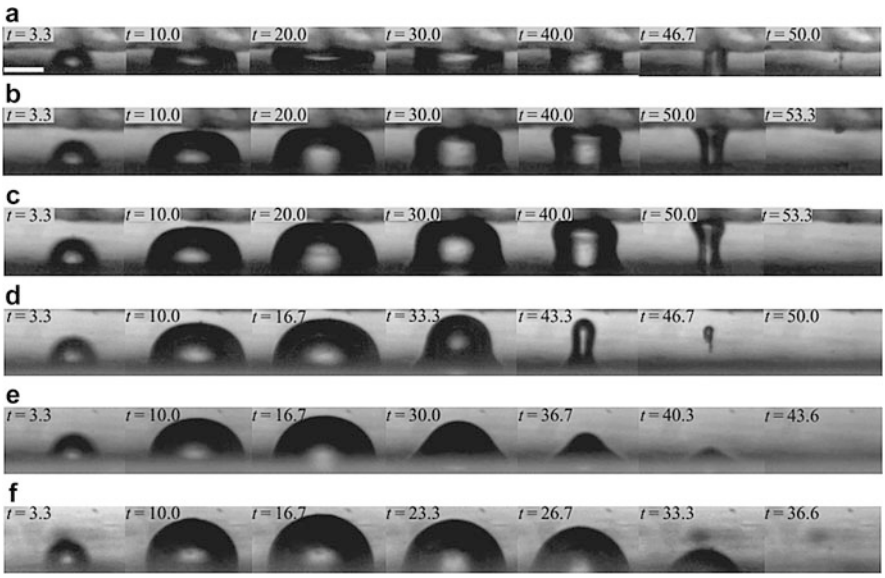

Fig. 9 Bubble dynamics as a function of channel height for bubbles with an approximate maximum horizontal bubble radius of $R_x = 140$ μm. The upper wall is visible in (**a**–**d**); the time in microseconds is shown on the *upper left* corner of each frame. (**a**) $\eta = h/R_x = 0.4$, bubble collapse between the two walls; (**b**) $\eta = 0.8$, bubble collapse onto the upper wall, at maximum expansion the bubble reaches the upper wall; (**c**) $\eta = 0.9$, bubble collapse onto the upper wall, the bubble does not reach the upper wall at maximum expansion; (**d**) $\eta = 1.2$, neutral collapse; (**e**) $\eta = 1.6$, non-spherical collapse onto the lower wall; and (**f**) $\eta = 7.3$, quasi-hemispherical collapse onto the lower wall. The scale bar indicates a length of 100 μm (Reproduced with permission from Ref. [45], Fig. 3)

discussed. First we will show the effect of the cavitation bubble dynamics on soft objects such as gas bubbles, biological cells, and droplets. Then an application will be presented to characterize the stiffness of some of the hardest fabricated material.

Interaction with Gas Bubbles

Gas bubble shock wave interaction is of major concern in medical applications such as shock wave lithotripsy [48–50], in cavitation damage research [44, 51], and in the study of explosives [52, 53]. In 2006, Chen et al. [13] devised a clever experiment where they generated first a gas bubble and then a cavitation bubble with a pulsed laser in a narrow gap filled with a light-absorbing liquid. The narrowness of the gap allowed a clear flow on the surface deformation, jetting, and breakup of the bubble resembling a cross-sectional cut; see Fig. 12. In a follow-up paper by Chen and Lin [54], they discussed the detailed fragmentation dynamics, yet more studies and comparison with analytical modeling of the fragmentation mechanics as well with numerical simulations may allow to make significant impact on our current understanding of shock wave–bubble interactions in liquids [55].

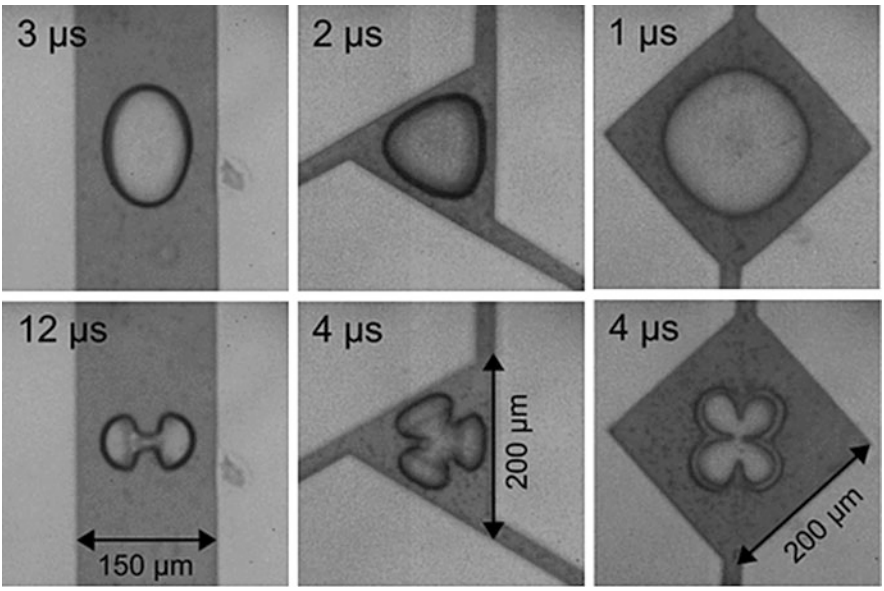

Fig. 10 Snapshots for three different geometries from *left* to *right*: single-bubble cavitation in a 150 µm wide and several millimeter long channel, in a 200 µm isosceles triangular structure with feeding channel attached to the corners and in a square chamber with 200 µm long sides (Reproduced with permission from Ref. [46], Fig. 5)

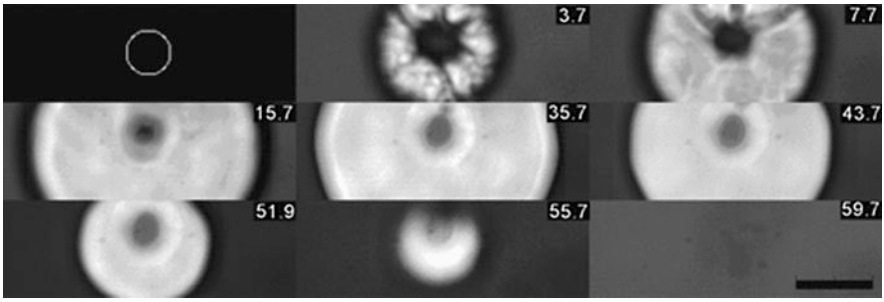

Fig. 11 Toroidal bubble created from a circular focus depicted in the first frame. The bubble expands initially with a rough surface likely due to separate bubbles which only coalesce in a later stage. Please note that the bubble retains its toroidal shape during the expansion and collapse cycle. The recording is taken at a frame rate of 250,000 fps. The black bar denotes a length of 100 µm and the time stamps in the *upper right* are given in microseconds (Reproduced with permission from Ref. [47], Fig. 8)

Interaction with Cells

The delivery of therapeutic agents into eucaryotic cells is hindered by the high selectivity of the cell membrane on foreign agents. In particular, uptake of large molecules such as DNA and RNA needs some active injection mechanics which

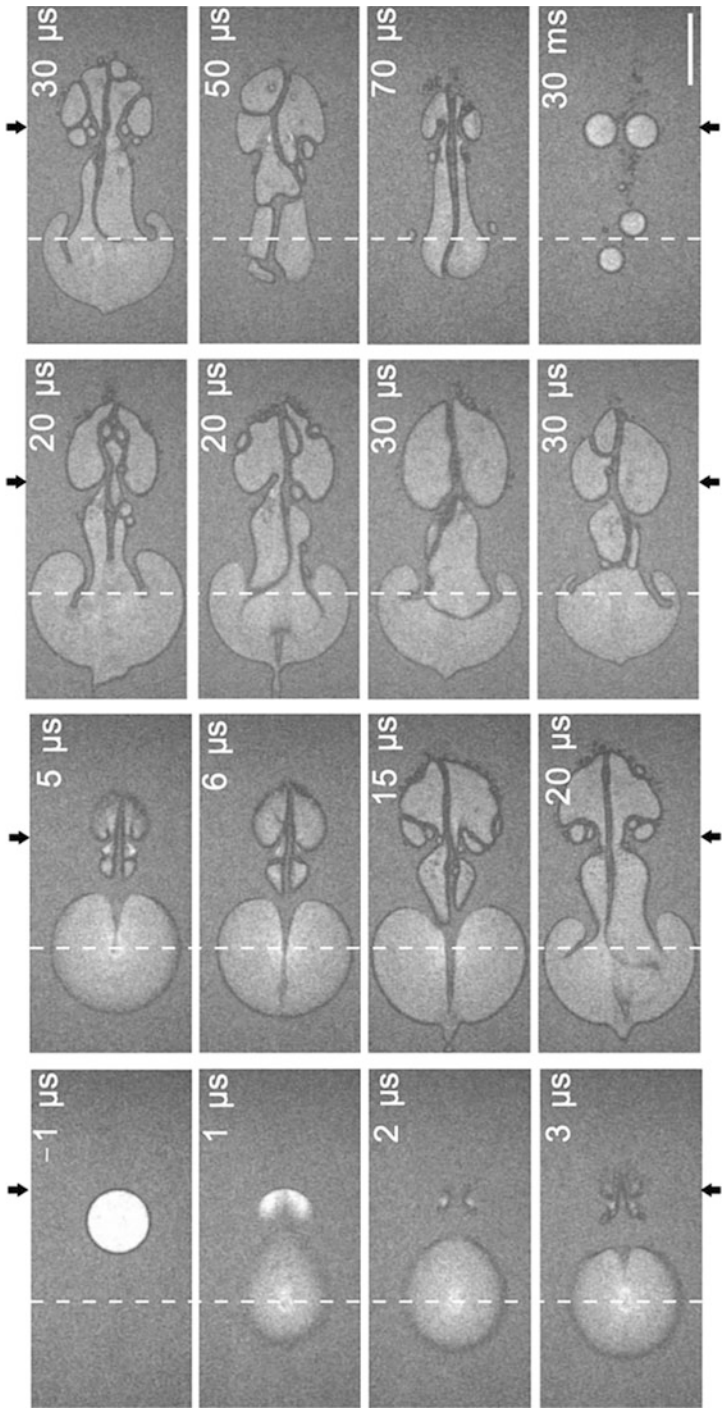

Fig. 12 Snapshots showing the bubble shape evolution for a gas bubble separated 0.225 mm from a cavitation bubble. The vertical dashed line and the arrows indicate the initial horizontal positions of the center of cavitation bubble and the right edge of the gas bubble, respectively. The length of the scale bar 0.2 mm (Reproduced with permission from Ref. [54], Fig. 12)

may be provided by viruses to deliver the molecular load through the plasma membrane. Transfecting single cells on demand would be a helpful tool in the development of novel medication and several approaches exist. Single-cell electroporation [56], optoporation [57], and sonoporation [58] have been developed. The latter two are based on focused laser light to directly form a tiny hole in the membrane and on creating/driving a bubble near to a cell to induce sufficient shear [58]. While in general the term sonoporation is used for driving a stable microbubble by ultrasound, they can also be generated with focused laser light in a microfluidic chip [59]. The technique has been considerably advanced using two laser pulses triggered at different times to create two bubbles with a high-speed jet [15, 60]. This tandem bubble technique has been carefully analyzed in the bulk liquid by Han et al. [61].

If the cavitation bubble is created within the cell, e.g., by focusing the laser pulse directly into the cell, cell lysis may be induced [62]. This technology may be suitable for collecting cellular content of single cells for μTAS systems. The strong shear flows (see section "Computational Fluid Dynamics (CFD) of Single Bubbles") created by an expanding cavitation can be utilized to test the rheological properties of cells. Quinto-Su et al. [63] demonstrated this in a study where original red blood cells were compared to cells that have been treated biochemically to soften and harden the plasma membrane. This nearly impulsive stretching of cells near to a cavitation bubble in a confined geometry can probe the cell's yield strength. Interestingly, maximum areal strain of a red blood cell is about an order of magnitude larger as compared to a quasi-static stretching [64, 65].

Generation and Coalescence Droplets

A pulsed laser-based droplet generator has been demonstrated by Park et al. [66]. The device consists of two parallel channels in which two immiscible fluids are flowing. They are connected by a nozzle and the laser is focused in one of the channels close to the nozzle. The expanding bubble accelerates some fluid into the second channel, thereby creating a droplet. The droplet size can be varied by changing the location of the laser focus and the laser energy allowing to produce highly repeatable droplets at rates of up to 10 kHz.

Having already a train of droplets and focusing a laser into that train, coalescence can be induced by the expanding bubble driving the interfaces into each other. Once the continuous phase separating the droplets ruptures coalescence is obtained. This technique has been demonstrated for on-demand droplet merging by Li et al. [67].

Interaction with Nano Objects

Two bubbles created simultaneously side by side in a microfluidic channel develop a liquid jet pointing toward each other, very similar to a single bubble created at half the distance to a rigid boundary. However, if one of the bubbles is considerably smaller, it will collapse and develop the jetting flow first. Once the second bubble collapses, it does not "see" the smaller collapsed bubble and shrinks more radially symmetric. The result is a directed flow from the smaller bubble to the larger bubble toward a stagnation point. A long object with dimensions oriented normal to the jet

flow direction will experience a largely nonuniform force which will bend the object. This allows to measure the elastic properties of suspended objects, such as multiwalled carbon nanotubes [68] and copper nanowires [69].

Generation of Fundamental Microfluidic Flows

A wide variety of flows can be generated by single and multiple bubbles. As described above, these flows can be used to separate cells, generate droplets, and deform thin objects. In microfluidic designs fundamental flows are combined to solve specific tasks. Here we'll provide a summary of fundamental flows cavitation bubbles can generate, i.e., mixing, pumping, switch, and cavitation induction. These flows may be combined, scaled, and optimized to solve a more complex microfluidic handling task.

Mixing

Mixing of miscible and low-viscosity fluids on large scale is a simple task; here the turbulent eddies support the entrainment the fluids such that molecular diffusion is occurring on a large interface. In microfluidics, surface forces keep flows even at rather high velocity laminar and therefore diffusion can only act on small interfacial areas. There are various ways to create these entraining eddies in microfluidics, one of them is to utilize the flow created by single cavitation bubbles. In the work of Hellman et al. [70], the horseradish peroxidase-catalyzed reaction is utilized to demonstrate rapid mixing after the collapse of a cavitation bubble. The bubble dynamics and liquid motion are shown in Fig. 13. Here two jets from along the channel direction meet and create a region of strong vorticity. This vortex region spreads and mixes both liquids over a timescale of milliseconds.

Pumping

When a cavitation bubble is expanding and collapsing in a channel, the location of expansion and collapse may differ if the bubble experiences different pressure boundary conditions during expansion (outflow of the tube into the reservoirs) and collapse (inflow). The reason is that for a finite Reynolds number, a jetting flow is generated during the bubble expansion, while during bubble collapse a sink flow is developed. Yuan et al. [40] model the flow for an arbitrary number of bubbles oscillating in the tube. They show that a single bubble being positioned not at the midpoint of the tube will create a net flow over one oscillation cycle, i.e., pump liquid to the side posing the lower resistance. The model has been refined by Ory et al. [41] considering the heat transfer and axisymmetric viscous flow.

A different pumping mechanism was used by Dijkink et al. [16]; they create a single bubble in chamber near to the exit channel. The channel width is considerably smaller than the chamber dimensions and the bubble at maximum expansion. Therefore the bubble dynamics is only little affected by the channel and shows a similar behavior as if it would collapse near a rigid boundary (see [71]): during bubble expansion it pushes some liquid into the channel; during early collapse,

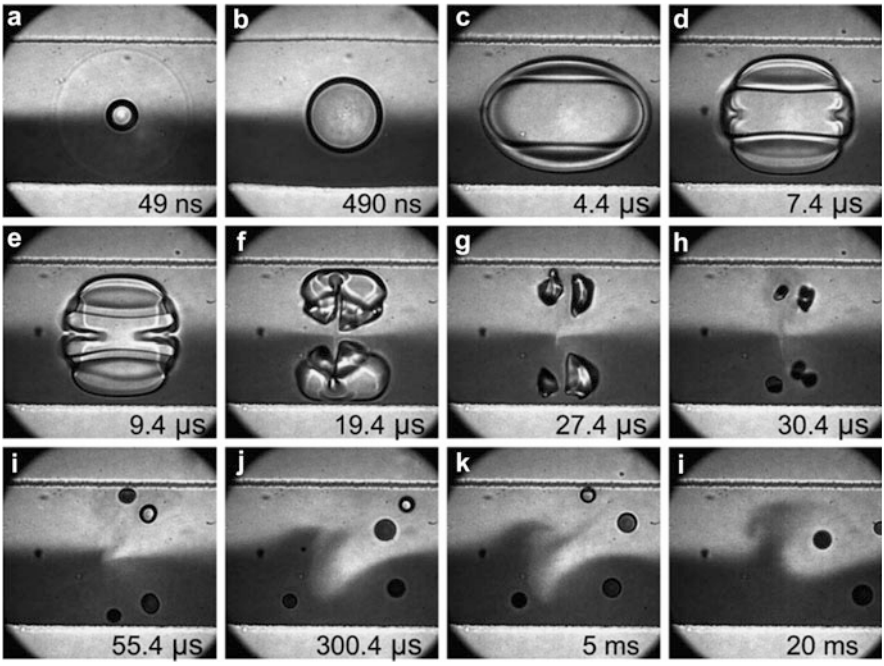

Fig. 13 Stroboscopic image series of a cavitation bubble expanding and collapsing and the subsequent mixing in a 200 µm wide microfluidic channel (Reproduced with permission from Ref. [70], Fig. 3)

liquid is sucked back into the chamber; and once the jet forms, liquid is pushed again into the chamber (Fig. 14). A net flux into the channel remains, resembling a positive displacement pump.

Switching and Sorting

Rapid switching of fluid flows allows the sorting of a stream of particles or droplets on demand. Wu et al. [72] demonstrated that a stream of particles can be deflected using the pressure generated from an expanding cavitation bubble. Their key idea is to separate the flow to be switched from a stagnant actuator chamber through an elastic membrane. Once a bubble is nucleated in the actuator chamber, it blocks the main flow which enters a y-region. At a suitable deflection strength, the particles or droplets can be switched between the two exit channels; see Fig. 15. This flow sorter was developed into a fluorescence cell sorter by Wu et al. [73].

Homogeneous Cavitation

During the early state of a violently expanding bubble, a shock wave is emitted which can be utilized for localized nucleation of secondary cavitation. An example of the shock wave emission is shown in frame (a) of Fig. 13. The initial pressure close to the bubble is of the order of gigapascals [74]. However it quickly drops to much lower pressures over time.

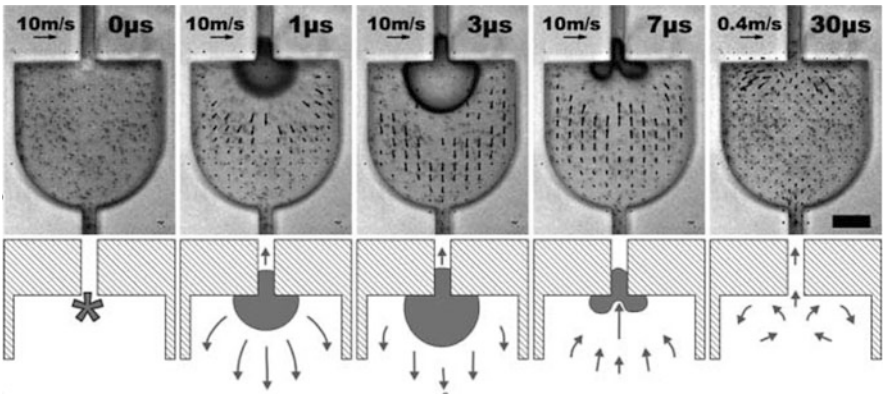

Fig. 14 Selected frames depicted the working principle a single bubble base pump displaying the microfluidic chamber (*below*), the bubble, and the channel (*on top*) into which the liquid is pumped. Overlayed are measured velocity vectors of the flow fields and a representation of the flow field is sketched below. The first image shows the chamber just before bubble initiation; 1 μs later the bubble is rapidly expanding, reaching its maximum size at 3 μs. Afterward the bubble starts to collapse creating a jet which is directed into the channel. In the last frame, the bubble has completely disappeared leaving some recirculating flow. The scale bar denotes 50 μm (Reproduced with permission from Ref. [71], Fig. 2)

Nucleation of secondary cavitation can be induced if the homogeneous cavitation threshold of the liquid is overcome. Although the precise value and the thermodynamic pathway for yield/rupture of water have not been settled [75], it is of the order of several hundreds of megapascals. The positive pressure pulse from the expanding bubble can be inverted by reflecting it at an acoustically soft boundary, e.g., a liquid–gas interface. The interface can be static as was shown in Ando et al. [74] or that of a neighboring expanding cavitation bubble as demonstrated by Quinto-Su and Ando [76]. In both cases the onset of homogeneous cavitation was found at -60 MPa and -20 MPa, respectively.

Applications Involving Bubbles in Confinement

In this section we present a brief discussion of a number of applications involving bubbles oscillating in a microfluidic environment. We focus on novel applications, such as using the ultrasonic bubbles to generate emulsions, and common biomedical applications involving cells.

Emulsification

When the cavitation bubbles in a microfluidic channel are excited strongly, they are capable of breaking up interfaces or fluid boundaries in a microfluidic channel or

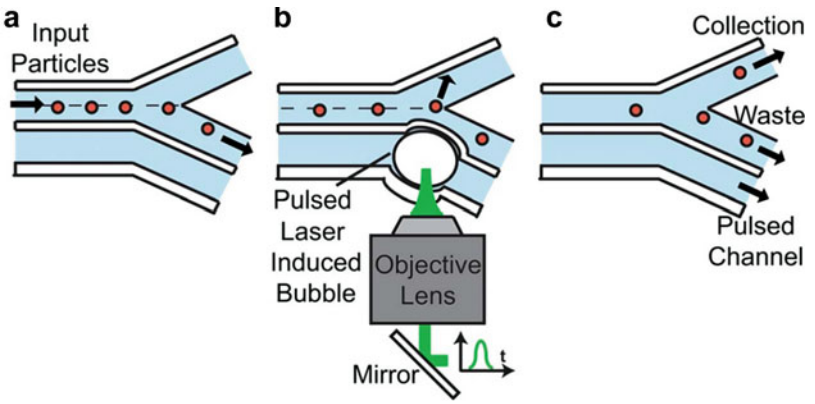

Fig. 15 Working principle of the cavitation bubble-based microfluidic switch. (**a**) Before switching, a train of particles/drops are transported into the waste channel. (**b**) A cavitation bubble is induced in the actuation chamber (pulsed channel) by a focused pulsed laser beam. The bubble expansion deforms the thin membrane and squeezes the fluid in the sample channel. (**c**) The selected particle is transported into the collection channel (Reproduced with permission from Ref. [72], Fig. 1)

chamber. Ohl et al. [21] report the use of the strongly oscillating bubbles to generate emulsions. Their setup is similar to that in Fig. 2 with the addition of a second liquid inlet. The two liquids are typically immiscible (e.g., oil and water) but not necessary so. The bubbles are generated as previously discussed (section "Ultrasound Contrast Agents"). However, in this case, there is an additional liquid–liquid interface.

Figure 16 shows the creation process of oil–water emulsion (viscosity ratio = 10:1). The liquid lining the microchannel is colored water, and a silicone oil is in the middle of the channel. The bubbles oscillate violently when the system is sonicated at its resonant frequency of about 100 kHz (driving voltage is about 200 V). They move along the channel rupturing the liquid–liquid interface, by creating high shear stress when oscillating and high-speed jets when collapsing. This process creates droplets in the channel. Further sonication causes the droplets to fragment into smaller droplets. It is found that the duration of ultrasound exposure is positively correlated to the uniformity of the emulsion and inversely correlated to the size of the droplets.

This system is highly efficient as submicron monodispersed emulsions as shown in Figs. 17 and 18 are created within milliseconds. Figure 17 shows a uniform emulsion of water in oil. Each of the droplet is about 1 μm in radius. A similar emulsion of oil in water is given in Fig. 18. In this case, the emulsion is slightly less uniform but longer sonication duration may increase the uniformity of the droplets formed. The system is highly versatile as emulsion of liquids with viscosity ratio up to 1000 has been produced.

Kentish et al. [77] use a sonic horn to generate nano-size droplets to form oil-in-water emulsions in a microfluidic chamber. Many other microfluidic emulsion generation systems make use of flow focusing instead on ultrasound and bubbles.

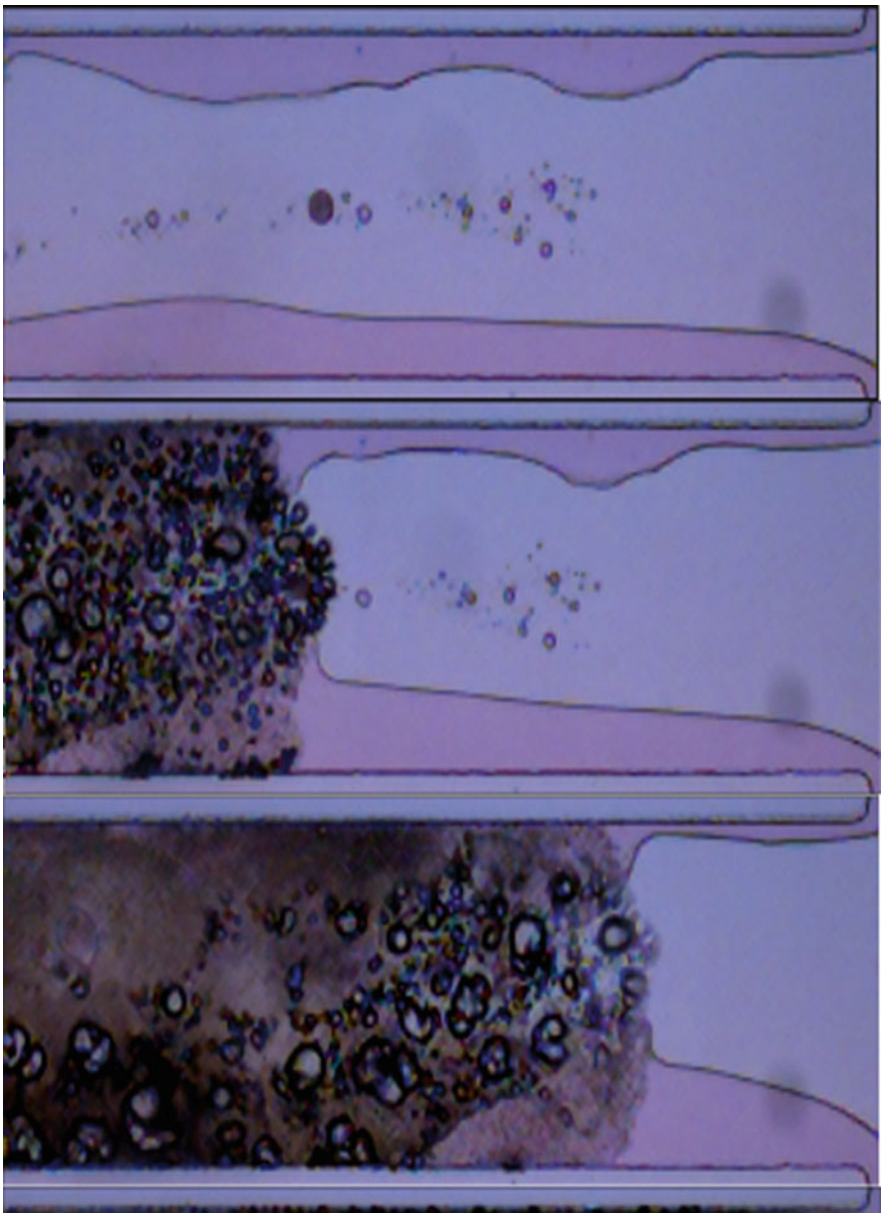

Fig. 16 The process of generating a water-in-oil emulsion. The bubbles are created as described in [10]. The flow in the channel induces the bubbles to move. They rupture the liquid–liquid interfaces, and droplets are formed

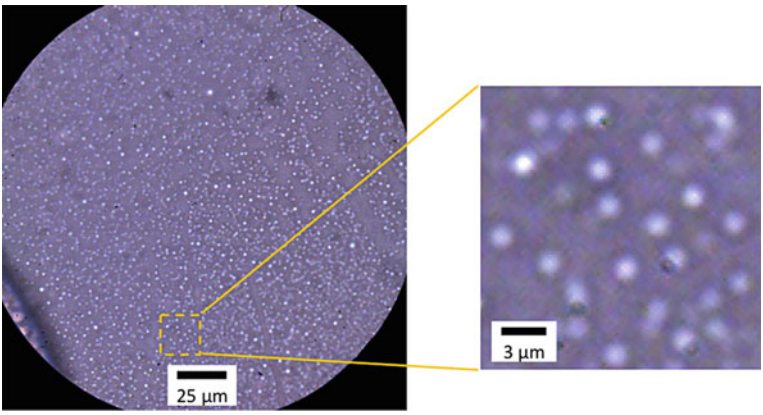

Fig. 17 Water-in-oil emulsion created in the microfluidic channel after sonification. The oil–water viscosity ratio is 100. The sub-figure on the *right* shows a magnified view of the area indicated

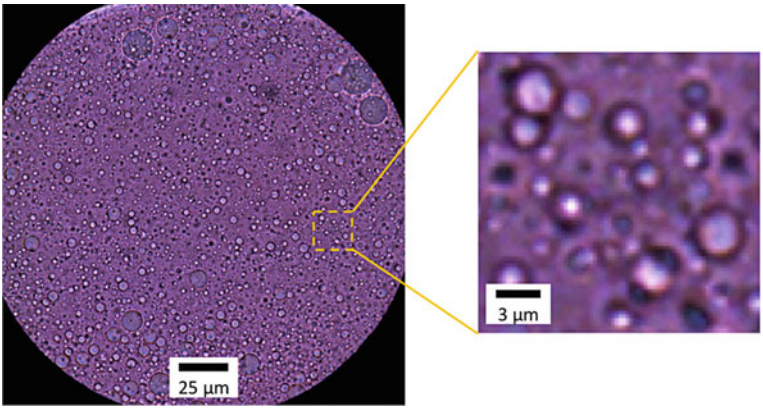

Fig. 18 Oil-in-water emulsion created in a microfluidic channel. The oil–water viscosity ratio is 100. The sub-figure on the *right* shows a magnified view of the region indicated

Some designs generate droplets through edifies or gaps in the microchannel, and others make use of mechanical parts such as a rotor to fragment the droplets. Recent reviews [78, 79] give good summaries of the current state of technology involved in the generation of emulsions in microfluidics.

Sonochemistry and Sonoluminescence

The strongly oscillating bubbles in a microfluidic channel generate transient regions of high temperature and pressure. Temperatures as high as 5000 °C and pressure as

high as 500 MPa have been measured [80]. The enormous energy concentrations in localized positions (where the bubbles collapse) enable chemicals to overcome reaction energy barrier. This branch of chemistry is known as sonochemistry. Sonochemistry is usually performed in bulk solution (within chemical flasks) using sonic horns. It is difficult to induce sonochemistry in microfluidics, due to the small volume of fluid and the problem of generating ultrasonic cavitation bubbles within the channels. Tandiono et al. [6] report the first success in generating chemiluminescence and sonoluminescence in microfluidics using a similar setup as described in Fig. 2.

The chemiluminescence described in [11] is the emission of light from the oxidation of luminol in a sodium carbonate base solution [81, 82]. The oxidation process is caused by the radicals H and OH which are produced by the ultrasonic bubbles from water (H_2O). The radicals subsequently trigger the formation of an unstable amino phthalate derivative with electrons in an excited state. As the chemical relaxes to lower-energy states, excess energy is emitted as a visible bluish light.

The image of the blue light emitted from chemiluminescence of luminol is captured by an intensified and cooled CCD camera (Fig. 19). The light is seen at the location where the cavitation bubbles are located (at the gas–liquid interfaces). The gray outline of the microfluidic channels which is taken with side illumination is superimposed to indicate the channel location. The green dash lines overlaid show the locations of the liquid slug.

Tandiono et al. [11] also show the evidence for sonoluminescence in their microfluidic system when it is strongly driven (driving voltage = 230 V). Sonoluminescence is the emission of light from the rapid heating of the bubble interior (during ultrasonic bubble collapse) without the use of chemicals. Figure 20 shows the light emission as detected by a photomultiplier. The microfluidic system is excited 100 times with 5000 cycles of ultrasound waves (on–off ratio is 0.01). It is noted that the amount of light detected in the sonoluminescence experiment is much lower than that from the chemiluminescence experiment. This is perhaps due to the fact that only a few of the bubble which collapses in the confined geometry of the microfluidic channels are sufficiently strong to induce sonoluminescence.

In a larger container, Rivas et al. [83] measure luminol chemiluminescence and sonoluminescence emission due to the oscillation and collapse of multiple bubbles generated from micromachined pits (15 μm in radius). Ultrasound is generated by a transducer placed at the bottom of a disk-shaped reactor and coupled to the glass bottom of the reactor. The plates containing the pits are arranged in several configurations and are submerged in the reactor and sonicated with different solutions. They report that the light emission is due to the transient cavitation nucleated by the microbubbles in the pits.

Tuziuti [84] investigate the effect of dissolved gas degree of saturation (DOS) on sonochemistry in a single microfluidic channel compared to a reactor which is millimeter in size. He measures the chemiluminescence intensity and finds that the sonochemical reaction in the microchannel needs lower power density for the same unit volume output. The 3D reactor requires higher power density and lower DOS to

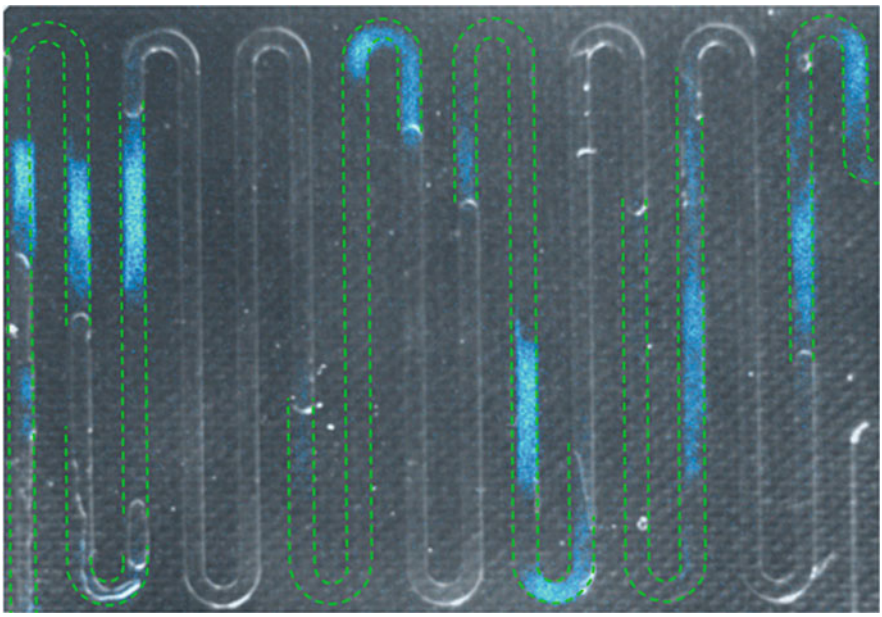

Fig. 19 Luminol chemiluminescence from cavitation bubble in microfluidic channels. The superimposed gray outline of the channel shows the distribution of the liquid and gas phases. The *green lines* indicate the locations of the liquid slugs. The bluish light from the oxidation of luminol is captured with an intensified and cooled CCD camera (Reproduced with permission from Ref. [11], Fig. 2a)

allow effective cavitation oscillations. He postulates that sonochemistry is more efficient and homogeneous in a microchannel.

Sonochemistry in microfluidics has the advantage of requiring only small amount of chemical fluids. The geometry allows direct observation of the relation between the ultrasonic bubbles, the sonochemistry, and the emission of light. The flexibility in microfluidic system design allows further optimization of these processes and customizations required for specific applications.

Biomedical Applications

Apart from chemistry-related applications, ultrasonic bubbles are utilized in various biomedical-related application of microfluidics. The small size of the channels is ideal for visualization of the manipulation of small objects such as cells and DNA. The controlled flow and ultrasound deployment allow for gentle handling of cells as well as applying localized shear stresses for cell lysis and fragmentation. In this section, several applications involving bacteria, yeast cell, red blood cells, and other biological tissues are discussed.

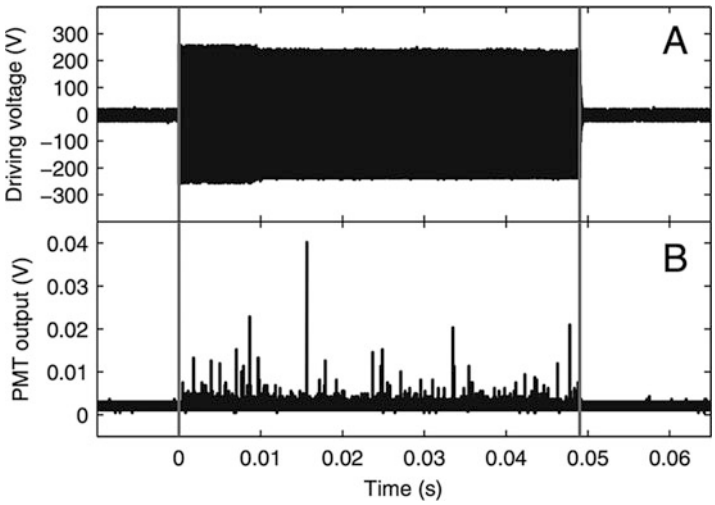

Fig. 20 Sonoluminescence signal from the microfluidic channels. (**a**) A driving voltage of 230 V is applied for 5000 cycles at the frequency of 103.6 kHz. (**b**) The light emission recorded by the photomultiplier from 100 repeated signals of (**a**). The light emission stops as soon as the ultrasound is turned off (Figure reproduced with permission from Ref. [6], Fig. 4)

Cell Stretching and Rupture

The harvesting of cellular content for analysis and profiling is an important process in biotechnology. Currently sonication is done in bulk medium using a vibrating probe which is inserted directly into the medium [85]. The ultrasound from the probe creates cavitation bubbles which oscillate and collapse. These bubbles generate mechanical shear stress on the cells and lyse them [86]. However this process is inefficient as some energy is lost as heat, and large amount of cells (medium in milliliter) is required.

Using microfluidics, however, the process is potentially more controlled. The cells could be lysed by different means in a microfluidic system: chemical [87], thermal [88], electrical [89], or mechanical [90]. Tandiono et al. [19] describe the use of a mechanical lysis of *Escherichia coli* bacterium and *Pichia pastoris* yeast cells using ultrasound in microfluidics. The gram-negative bacterium and the yeast cells are chosen because they are common microbial host cells that are used for screening of clones from genomic libraries and heterologous protein expression [91, 92]. Both cells allow the functional expression of multiple proteins in parallel in microplate assay. These proteins can be made amenable to microscale analysis.

The microfluidic system used in the experiment consists of a meandering channel, with two inputs (one for gas and one for liquid), and an outlet similar to the one in Fig. 2. The cells are mixed with the input liquid before the liquid comes into contact with the gas to form a slug after the T-junction. The main channel has a width of 500 μm and a depth of 20 μm. The ultrasound is generated by four transducers which are attached on the same glass slide as the PDMS (polydimethylsiloxane) slab

containing the microfluidic channels. Sonication is done in burst with 5-second intervals. The transducer is driven with 200 V at resonant frequency of the system (~130 kHz).

The effect of the sonication on the green fluorescent protein (GFP) expressing *E. coli* is shown in Fig. 21. Before the ultrasound is applied (Fig. 21a, left), the rod-shaped bacteria are seen to fluoresce in green. During sonication, the fluid movement and intense interaction between the bubbles and the cells are shown in the motion-blurred Fig. 21a (center). After the ultrasound is turned off, the flow in the channel stops. However it is clear that no intact bacteria remain (Fig. 21a, right). The supernatant appears greenish with the intracellular content from the lysed cells. Bright field microscopy (Fig. 21b) shows the microfluidic channel with the bacteria (left). After sonication, all of the bacteria are fragmented (right).

Tandiono et al. [19] also sonicate *Pichia pastoris* yeast cells using the same microfluidic system. The yeast cells harboring the pAcGFP1 (Clontech) and pGAP-EGFPd vectors are used. These cells have rigid extracellular cell wall which is made of a layered mesh of embedded glucans, chitin, and mannoproteins. The cell wall provides structural support that makes the yeast cell difficult to lyse.

Figure 22 shows the amount of DNA (deoxyribonucleic acid) released from the *P. pastoris* over time as quantified using qRT-PCR (real-time polymerase chain reaction) analysis. Both axes are logarithmically scaled. With longer sonication, the DNA concentration increases. It levels off after about 1 second. Further sonication leads to a decrease in DNA concentration measured. This may be an indication of DNA damage due to chemical exposure (such as the OH radicals) [11] or mechanical shear stress.

Marentis et al. [93] use a microfluidic ultrasound system, which they term microsonicator, to lyse mammalian cells (HL-60) and bacterial spores (*Bacillus subtilis*). The microfluidic channel used in [93] is 500 μm in width and 500 μm in height. It is sonicated from below by an attached transducer at 380 MHz. They report that 77.5 % of the HL-60 cells are lysed at a flow rate of 50 L/min. For the more difficult to lyse spores, at 5 L/min, 54 % of the *B. subtilis* spores are lysed. Many other microfluidic systems for cell lysis do not make use of ultrasound [94].

Another application of ultrasonic microfluidic system is for sorting and separation of cells or blood content [95–97]. In these systems standing waves are utilized. Augustsson et al. [95] use acoustophoresis to separate prostate cancer cells from white blood cells. Yang and Soh [96] develop an ultrasonic microfluidic system that sorts viable cells from a cell mixture containing both viable and nonviable cells. Ding et al. [97] use precisely controlled standing surface acoustic wave (SSAW) multichannel microfluidic system for cell sorting and processing. It is noted that these applications do not make use of ultrasonic bubbles.

When a laser-generated bubble is oscillating next to a red blood cell (RBC), it has been shown that the cell can be stretched [63] (also see Section "Interaction with Cells"). Tandiono et al. [20] extend the study by observing the interaction between one RBC and a single laser-generated cavitation bubble in a microfluidic chamber. The cell is placed in a microchamber which has a height of 20 μm. A pulsed laser is used to generate the cavitation bubble. Figure 23 shows the cell's response next to

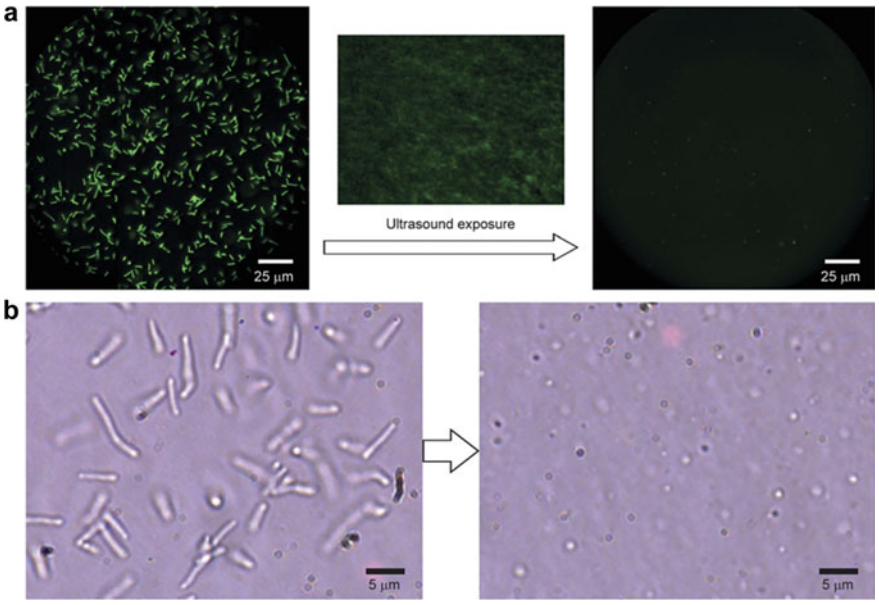

Fig. 21 Images of green fluorescent protein (GFP) *Escherichia coli* taken before and after sonication. (**a**) Fluorescence microscopy imaging of the bacteria before (*left*), during (*middle*), and after (*right*) ultrasound exposure. All bacteria are lysed with supernatant which appears greenish due to the intracellular content. (**b**) Bright field microscopy images of the bacteria before (*left*) and after (*right*) sonication. All bacteria are fragmented (Figure reproduced with permission from Ref. [19], Fig. 2)

the bubble. Initially (frame 1), the cell (4 μm in radius) is 84 μm away from the bubble center. As the bubble expands, the bottom of the cell is pushed away and the cell appears being "flattened" (frames 2–4). The bubble reaches its maximum size (100 μm in radius) at frame 4. After which, the bubble collapses. The flow generated by the rapid collapse of the bubble causes the RBC to stretch. Eventually it is seen to be elongated (frame 12).

Tandiono et al. [20] attempt to understand the stretching mechanism with numerical simulation. A boundary element method code is used to simulate the interaction of an elastic fluid vesicle and a vapor bubble. Details of the modeling methodology are reported in previous publications [98, 99]. The elasticity on the cell is described by an elasticity parameter, K, where $K = \frac{\sigma}{R_c p_\infty}$, σ is the surface tension, R_c is the cell radius, and p_∞ is the ambient pressure. Figure 24 shows the result of a cell with moderate elasticity ($K = 0.067$). The cell is flattened at the bottom and pushed up slightly as the bubble expands. When the bubble collapses, the cell bottom is initially stretched, and the whole cell is elongated at the end of the collapse.

For a rigid cell with $K = 1.33$, there is hardly any deformation on the cell throughout the bubble oscillation. As shown in Fig. 25, the rigid cell undergoes mild oscillation and returns to its original round shape after the bubble has collapsed. For a very "soft" cell with no surface tension ($K = 0$), it deforms as the bubble

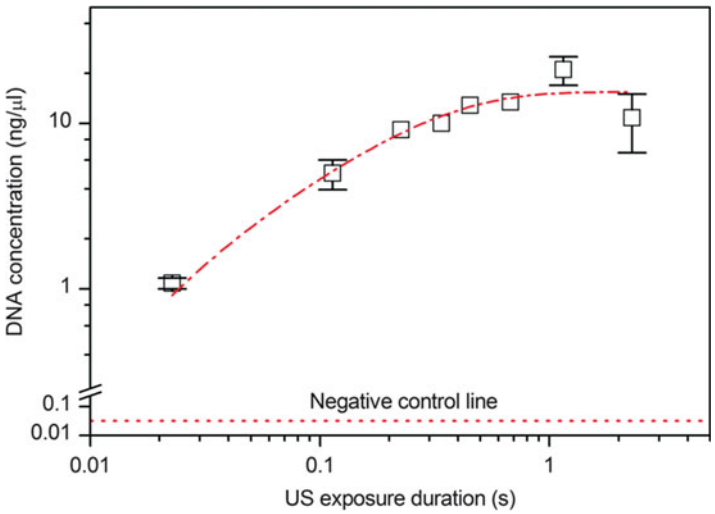

Fig. 22 DNA concentration of the treated *Pichia pastoris* yeast cell with increasing sonication. The error bars are obtained from multiple runs (2–4 runs). It is seen that DNA concentration increases with longer ultrasound exposure. After about 1 s, the amount of DNA levels is off. The negative control is obtained from untreated samples (Figure reproduced with permission from Ref. [19], (Fig. 6)

expands. But it regains its shape upon bubble collapse. From a parametric study, it is understood that only cells within certain elasticity range demonstrate the "stretching" phenomena. Also maximum elongation occurs when the oscillations of the bubble and cell are out of phase, that is, the bubble oscillates at half the oscillation time of the cell.

The ease of manipulating small entities, like cells, and the low volume of liquid needed (low-resource requirement) are important driving forces behind the use of microfluidics for biomedical technology. Diagnostic kits using microfluidics have been developed as a point-of-care device or as a substitute to the time-consuming laboratory testing [100–102] (note that no acoustic cavitation is used in these systems). For example, Chin et al. [100] use a microfluidic chip to perform ELISA-like assay for the detection of human immunodeficiency virus (HIV) in blood samples. The device requires only 20-minute processing time, needs small volume of blood (obtainable from a lancet puncture), and uses cheap photodetectors for rapid optical readout. Tests done using patient blood samples from a hospital in Rwanda show results that match the sensitivity and specificity of a rival laboratory-based ELISA test. Another clinical use of microfluidics is in the rapid purification and analysis of neutrophils. Warner et al. [101] design and utilize a microfluidic chip to isolate human blood polymorphonuclear cells (PMNs). These cells are then analyzed for gene expression using a commercial GeneChips. The results show unique genomic expression among patients with acute respiratory distress syndrome (as compared to healthy control subjects). Kotz et al. [102] make a microfluidic chip that is capable of isolating neutrophils from whole blood samples and "on-chip"

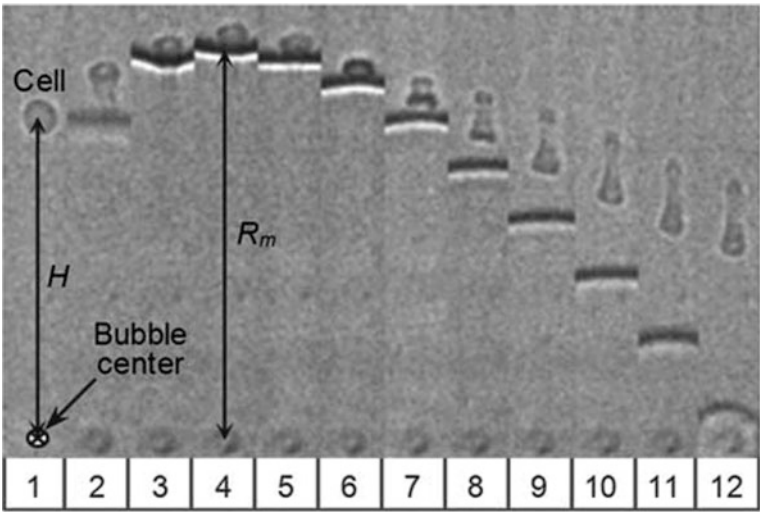

Fig. 23 A large cavitation bubble (partially seen) generated by a pulsed laser expands and collapses near a red blood cell. There are 12 frames shown taken at an interval of 2.78 ms (framing rate = 360,000 fps). The frame width is 16 μm. The cell is "flattened" during bubble expansion (frames 1–4) and then "stretched" during bubble collapse (Figure reproduced with permission from Ref. [20], Fig. 2)

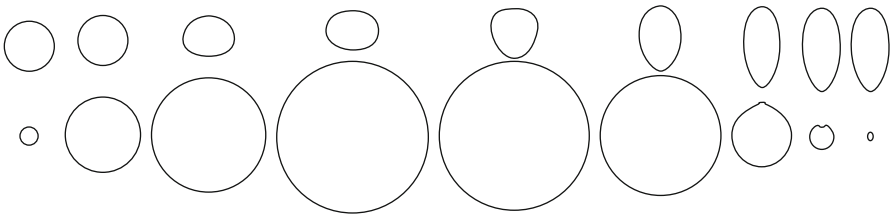

Fig. 24 Interaction of a "floppy" cell (*on top*) and a cavitation bubble (*below*). The cell has an elasticity parameter, $K = 0.067$. It is initially "flattened" when the bubble expands, and then it is "stretched" as the bubble collapses (Reproduced with permission from Ref. [20], Fig. 6)

processing for mRNA and protein isolation for genomics and proteomics. The device is tested on blood samples from trauma and burn patients with success. In conclusion, these microfluidic diagnostic techniques have the advantages of rapid processing, small sample volume requirement, and low-cost.

Conclusions

In general, the use of microfluidics as a research investigative tool has been expanded to practical and commercial products in recent years. It is used in fluid

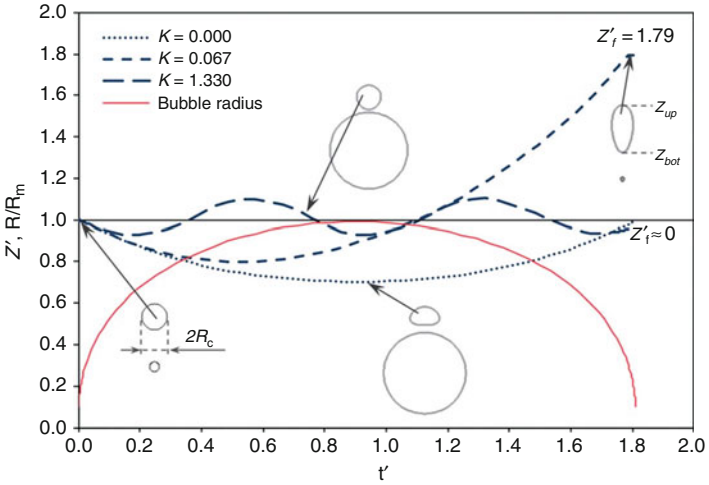

Fig. 25 The vertical deformation of the cell, Z', as a function of the dimensionless time, t': $Z' = \frac{z_{up} - z_{bottom}}{2R_c}$, where z_{up} is the top coordinate, and z_{bottom} is the lowest coordinate of the cell along the axis of symmetry, z. $t' = \frac{t}{R_m\sqrt{\rho_1/p_\infty}}$, where R_m is the maximum bubble radius, p_1 is the density of the fluid inside the cell, and p_∞ is the ambient pressure. The cell with no surface tension ($K = 0$) is flattened as the bubble expands but regains its shape upon bubble collapse. The rigid cell ($K = 1.33$) oscillates slightly as the bubble expands and collapses. Only the cell with moderate elasticity ($K = 0.067$) elongates after bubble collapses (Reproduced with permission from Ref. [21], Fig. 8)

dynamic studies for transport, sorting, mixing, emulsification, and the manufacturing of coated bubbles and droplets. It has also been used for chemical and biological analysis, clinical diagnostics, and treatment. In a 2006 *Nature* paper, Whiteside [103] has predicted that "(the) microfluidic technology will become a major theme in the analysis, and perhaps synthesis, of molecules." Indeed many microfluidic tools and systems have since been developed. However there are still limitations to be overcome, notably the lack of robustness and the difficulty in upscaling output volume. Most microfluidic devices that are made of PDMS (polydimethylsiloxane) are subjected to degradation after rapid use or thermal loading. The output volume of a microfluidic device is typically in the microliter, which is good for laboratory research or analysis but not practical for biotechnology processing and manufacturing. Nevertheless, it has remained an indispensable tool in scientific research. Its ability to facilitate visualization, its small input volume requirement, its potential for rapid processing and low-cost are advantages that will continue to fuel its development in the future.

A fruitful area for future study may be the simplification of current microfluidic designs which then would allow upscaling. Yet, to achieve this, electric engineers who are to integrate acoustic transducer, and fluid mechanics specialist and materials expert who are to design channels which can be mass produced, are needed. Then

instead of sonicating the bulk of a liquid with complex acoustics and bubble dynamics, simpler flows near to surfaces are obtained. We expect that breakthroughs in these geometries may be possible.

Acknowledgments The authors would like to acknowledge the following funding sources: A*STAR Joint Council Office Grants: 10/03/FG/05/02 and CCOGA02-014-2008.

References

1. Blake JR, Taib BB, Doherty G (1986) Transient cavities near boundaries. Part 1. Rigid boundary. J Fluid Mech 170:479–497
2. Best JP, Kucera A (1992) A numerical investigation of non-spherical rebounding bubbles. J Fluid Mech 245:137–154
3. Lauterborn W, Kurz T (2010) Physics of bubble oscillations. Rep Prog Phys 73(10):106501
4. Flynn HG (1975) Cavitation dynamics: II. Free pulsations and models for cavitation bubbles. J Acoust Soc Am 58(6):1160–1170
5. Mishra C, Peles Y (2005) Cavitation in flow through a micro-orifice inside a silicon microchannel. Phys Fluids 17(1):013601
6. Duan C, Karnik R, Lu M-C, Majumdar A (2012) Evaporation-induced cavitation in nanofluidic channels. Proc Natl Acad Sci 109(10):3688–3693
7. Wheeler TD, Stroock AD (2008) The transpiration of water at negative pressures in a synthetic tree. Nature 455(7210):208–212
8. Vincent O, Marmottant P, Quinto-Su PA, Ohl C-D (2012) Birth and growth of cavitation bubbles within water under tension confined in a simple synthetic tree. Phys Rev Lett 108 (18):184502
9. Taylor MT, Belgrader P, Furman BJ, Pourahmadi F, Kovacs GTA, Northrup MA (2001) Lysing bacterial spores by sonication through a flexible interface in a microfluidic system. Anal Chem 73(3):492–496
10. Tandiono, Ohl S-W, Ow DS-W, Klaseboer E, Wong VVT, Camattari A, Ohl C-D (2010) Creation of cavitation activity in a microfluidic device through acoustically driven capillary waves. Lab Chip 10(14):1848–1855
11. Tandiono, Ohl S-W, Ow DSW, Klaseboer E, Wong VV, Dumke R, Ohl C-D (2011) Sonochemistry and sonoluminescence in microfluidics. Proc Natl Acad Sci 108 (15):5996–5998
12. Xu J, Attinger D (2007) Control and ultrasonic actuation of a gas–liquid interface in a microfluidic chip. J Micromech Microeng 17(3):609–616
13. Chen Y-H, Chu H-Y, Lin I (2006) Interaction and fragmentation of pulsed laser induced microbubbles in a narrow gap. Phys Rev Lett 96(3):034505
14. Vogel A, Venugopalan V (2003) Mechanisms of pulsed laser ablation of biological tissues. Chem Rev 103(2):577–644
15. Sankin GN, Yuan F, Zhong P (2010) Pulsating tandem microbubble for localized and directional single-cell membrane poration. Phys Rev Lett 105(7):078101
16. Dijkink R, Ohl C-D (2008) Laser-induced cavitation based micropump. Lab Chip 8 (10):1676–1681
17. Suh YK, Kang S (2010) A review on mixing in microfluidics. Micromachines 1(3):82–111
18. Iida Y, Yasui K, Tuziuti T, Sivakumar M, Endo Y (2004) Ultrasonic cavitation in microspace. Chem Commun 20:2280–2281
19. Tandiono T, Ow DS-W, Driessen L, Chin CS-H, Klaseboer E, Choo AB-H, Ohl S-W, Ohl C-D (2012) Sonolysis of *Escherichia coli* and *Pichia pastoris* in microfluidics. Lab Chip 12 (4):780–786

20. Tandiono T, Klaseboer E, Ohl S-W, Ow DS-W, Choo AB-H, Li F, Ohl C-D (2013) Resonant stretching of cells and other elastic objects from transient cavitation. Soft Matter 9 (36):8687–8696
21. Ohl S-W, Tandiono T, Klaseboer E, Ow D, Choo A, Li F, Ohl C-D (2014) Surfactant-free emulsification in microfluidics using strongly oscillating bubbles. J Acoust Soc Am 136 (4):2289–2289
22. Frinking PJA, Bouakaz A, Kirkhorn J, Ten Cate FJ, De Jong N (2000) Ultrasound contrast imaging: current and new potential methods. Ultrasound Med Biol 26(6):965–975
23. Unger E, Porter T, Lindner J, Grayburn P (2014) Cardiovascular drug delivery with ultrasound and microbubbles. Adv Drug Deliv Rev 72:110–126
24. Ferrara K, Pollard R, Borden M (2007) Ultrasound microbubble contrast agents: fundamentals and application to gene and drug delivery. Annu Rev Biomed Eng 9:415–447
25. Hernot S, Klibanov AL (2008) Microbubbles in ultrasound-triggered drug and gene delivery. Adv Drug Deliv Rev 60(10):1153–1166
26. Datta S, Coussios CC, Ammi AY, Mast TD, de Courten-Myers GM, Holland CK (2008) Ultrasound-enhanced thrombolysis using Definity® as a cavitation nucleation agent. Ultrasound Med Biol 34(9):1421–1433
27. Taniyama Y, Tachibana K, Hiraoka K, Aoki M, Yamamoto S, Matsumoto K, Nakamura T, Ogihara T, Kaneda Y, Morishita R (2002) Development of safe and efficient novel nonviral gene transfer using ultrasound: enhancement of transfection efficiency of naked plasmid DNA in skeletal muscle. Gene Ther 9(6):372–380
28. Wu J, Xie F, Lof J, Sayyed S, Porter TR (2015) Utilization of modified diagnostic ultrasound and microbubbles to reduce myocardial infarct size. Heart 101:1468–1474
29. O'Reilly MA, Hynynen K (2015) Emerging non-cancer applications of therapeutic ultrasound. Int J Hyperthermia 31(3):310–318
30. Guo H, Leung JCK, Chan LYY, Tsang AWL, Lam MF, Lan HY, Lai KN (2007) Ultrasound-contrast agent mediated naked gene delivery in the peritoneal cavity of adult rat. Gene Ther 14 (24):1712–1720
31. Xiong S, Chin LK, Ando K, Tandiono T, Liu AQ, Ohl CD (2015) Droplet generation via a single bubble transformation in a nanofluidic channel. Lab Chip 15(6):1451–1457
32. Leighton TG (2011) The inertial terms in equations of motion for bubbles in tubular vessels or between plates. J Acoust Soc Am 130(5):3333–3338, New York
33. Luther S, Mettin R, Lauterborn W (2000) Modeling acoustic cavitation by a Lagrangian approach. In: AIP conference proceedings, IOP Institute Of Physics Publishing Ltd, New York pp. 351–354
34. Harkin A, Kaper TJ, Nadim A (2001) Coupled pulsation and translation of two gas bubbles in a liquid. J Fluid Mech 445:377–411
35. Ilinskii YA, Hamilton MF, Zabolotskaya EA (2007) Bubble interaction dynamics in Lagrangian and Hamiltonian mechanics. J Acoust Soc Am 121(2):786–795
36. Quinto-Su PA, Ohl C-D (2009) Interaction between two laser-induced cavitation bubbles in a quasi-two-dimensional geometry. J Fluid Mech 633:425–435
37. Elkouh AF (1975) Oscillating radial flow between parallel plates. Appl Sci Res 30(6):401–417
38. Von Kerczek CH (1999) A note about the radial diffuser. Acta mech 135(3–4):229–233
39. Li F, Mohammadzadeh M, Ohl CD (2013) Shear stress induced stretching of red blood cells by oscillating bubbles within a narrow gap. Bull Am Phys Soc 58
40. Yuan H, Prosperetti A (1999) The pumping effect of growing and collapsing bubbles in a tube. J Micromech Microeng 9(4):402
41. Ory E, Yuan H, Prosperetti A, Popinet S, Zaleski S (2000) Growth and collapse of a vapor bubble in a narrow tube. Phys Fluids 12(6):1268–1277
42. Ye T, Bull JL (2004) Direct numerical simulations of micro-bubble expansion in gas embolotherapy. J Biomech Eng 126(6):745–759
43. Ye T, Bull JL (2006) Microbubble expansion in a flexible tube. J Biomech Eng 128 (4):554–563

44. Philipp A, Lauterborn W (1998) Cavitation erosion by single laser-produced bubbles. J Fluid Mech 361:75–116
45. Gonzalez-Avila SR, Klaseboer E, Khoo BC, Ohl C-D (2011) Cavitation bubble dynamics in a liquid gap of variable height. J Fluid Mech 682:241–260
46. Zwaan E, Le Gac S, Tsuji K, Ohl C-D (2007) Controlled cavitation in microfluidic systems. Phys Rev Lett 98(25):254501
47. Lim KY, Quinto-Su PA, Klaseboer E, Khoo BC, Venugopalan V, Ohl CD (2010) Nonspherical laser-induced cavitation bubbles. Phys Rev E 81(1):016308
48. Delius M (1994) Medical applications and bioeffects of extracorporeal shock waves. Shock waves 4(2):55–72
49. Sankin GN, Simmons WN, Zhu SL, Zhong P (2005) Shock wave interaction with laser-generated single bubbles. Phys Rev Lett 95(3):034501
50. Johnsen E, Colonius T (2008) Shock-induced collapse of a gas bubble in shockwave lithotripsy. J Acoust Soc Am 124(4):2011–2020
51. Dowson D, Taylor CM (1979) Cavitation in bearings. Annu Rev Fluid Mech 11(1):35–65
52. Field JE (1992) Hot spot ignition mechanisms for explosives. Acc Chem Res 25(11):489–496
53. Saurel R, Lemetayer O (2001) A multiphase model for compressible flows with interfaces, shocks, detonation waves and cavitation. J Fluid Mech 431:239–271
54. Chen Y-H, Lin I (2008) Dynamics of impacting a bubble by another pulsed-laser-induced bubble: jetting, fragmentation, and entanglement. Phys Rev E 77(2):026304
55. Delale CF (ed) (2012) Bubble dynamics and shock waves, vol 8. Springer, Berlin, Heidelberg
56. Khine M, Lau A, Ionescu-Zanetti C, Seo J, Lee LP (2005) A single cell electroporation chip. Lab Chip 5(1):38–43
57. Stevenson DJ, Gunn-Moore FJ, Campbell P, Dholakia K (2010) Single cell optical transfection. J R Soc Interface 7(47):863–871
58. Annemieke VW, Kooiman K, Harteveld M, Marcia E, Folkert J, Versluis M, De Jong N (2006) Vibrating microbubbles poking individual cells: drug transfer into cells via sonoporation. J Control Release 112(2):149–155
59. Gac SL, Zwaan E, van den Berg A, Ohl C-D (2007) Sonoporation of suspension cells with a single cavitation bubble in a microfluidic confinement. Lab Chip 7(12):1666–1672
60. Hsiao C-T, Choi J-K, Singh S, Chahine GL, Hay TA, Ilinskii YA, Zabolotskaya EA, Hamilton MF, Sankin G, Yuan F, Zhong P (2013) Modelling single-and tandem-bubble dynamics between two parallel plates for biomedical applications. J Fluid Mech 716:137–170
61. Han B, Köhler K, Jungnickel K, Mettin R, Lauterborn W, Vogel A (2015) Dynamics of laser-induced bubble pairs. J Fluid Mech 771:706–742
62. Quinto-Su PA, Lai H-H, Yoon HH, Sims CE, Allbritton NL, Venugopalan V (2008) Examination of laser microbeam cell lysis in a PDMS microfluidic channel using time-resolved imaging. Lab Chip 8(3):408–414
63. Quinto-Su PA, Kuss C, Preiser PR, Ohl C-D (2011) Red blood cell rheology using single controlled laser-induced cavitation bubbles. Lab Chip 11(4):672–678
64. Li F, Chan CU, Ohl CD (2013) Yield strength of human erythrocyte membranes to impulsive stretching. Biophys J 105(4):872–879
65. Li F, Chan CU, Ohl CD (2014) Rebuttal to a comment by Richard E. Waugh on our article "Yield Strength of Human Erythrocyte Membranes to Impulsive Stretching". Biophys J 106 (8):1832
66. Park S-Y, Wu T-H, Chen Y, Teitell MA, Chiou P-Y (2011) High-speed droplet generation on demand driven by pulse laser-induced cavitation. Lab Chip 11(6):1010–1012
67. Li ZG, Ando K, Yu JQ, Liu AQ, Zhang JB, Ohl CD (2011) Fast on-demand droplet fusion using transient cavitation bubbles. Lab Chip 11(11):1879–1885
68. Quinto-Su PA, Huang XH, Gonzalez-Avila SR, Wu T, Ohl CD (2010) Manipulation and microrheology of carbon nanotubes with laser-induced cavitation bubbles. Phys Rev Lett 104 (1):014501

69. Huang X, Quinto-Su PA, Gonzalez-Avila SR, Wu T, Ohl C-D (2010) Controlled manipulation and in situ mechanical measurement of single co nanowire with a laser-induced cavitation bubble. Nano Lett 10(10):3846–3851
70. Hellman AN, Rau KR, Yoon HH, Bae S, Palmer JF, Phillips KS, Allbritton NL, Venugopalan V (2007) Laser-induced mixing in microfluidic channels. Anal Chem 79(12):4484–4492
71. Lew KSF, Klaseboer E, Khoo BC (2007) A collapsing bubble-induced micropump: an experimental study. Sensors Actuators A Phys 133(1):161–172
72. Wu T-H, Gao L, Wei K, Chiou EPY (2008) Pulsed laser triggered high speed microfluidic switch. In: Optical MEMs and nanophotonics, 2008 IEEE/LEOS International conference on, IEEE, pp. 19–20
73. Wu T-H, Chen Y, Park S-Y, Hong J, Teslaa T, Zhong JF, Di Carlo D, Teitell MA, Chiou P-Y (2012) Pulsed laser triggered high speed microfluidic fluorescence activated cell sorter. Lab Chip 12(7):1378–1383
74. Ando K, Liu A-Q, Ohl C-D (2012) Homogeneous nucleation in water in microfluidic channels. Phys Rev Lett 109(4):044501
75. Azouzi MEM, Ramboz C, Lenain J-F, Caupin F (2013) A coherent picture of water at extreme negative pressure. Nat Phys 9(1):38–41
76. Quinto-Su PA, Ando K (2013) Nucleating bubble clouds with a pair of laser-induced shocks and bubbles. J Fluid Mech 733:R3 (12 pages)
77. Kentish S, Wooster TJ, Ashokkumar M, Balachandran S, Mawson R, Simons L (2008) The use of ultrasonics for nanoemulsion preparation. Innovative Food Sci Emerg Technol 9 (2):170–175
78. Maan AA, Schroën K, Boom R (2011) Spontaneous droplet formation techniques for monodisperse emulsions preparation–perspectives for food applications. J Food Eng 107 (3):334–346
79. Zhao C-X (2013) Multiphase flow microfluidics for the production of single or multiple emulsions for drug delivery. Adv Drug Deliv Rev 65(11):1420–1446
80. Suslick KS (1990) Sonochemistry. Science 247(4949):1439–1445
81. Henglein A, Ulrich R, Lilie J (1989) Luminescence and chemical action by pulsed ultrasound. J Am Chem Soc 111(6):1974–1979
82. Hatanaka S-i, Mitome H, Yasui K, Hayashi S (2002) Single-bubble sonochemiluminescence in aqueous luminol solutions. J Am Chem Soc 124(35):10250–10251
83. Fernandez Rivas D, Ashokkumar M, Leong T, Yasui K, Tuziuti T, Kentish S, Lohse D, Gardeniers HJGE (2012) Sonoluminescence and sonochemiluminescence from a microreactor. Ultrason Sonochem 19(6):1252–1259
84. Tuziuti T (2013) Influence of degree of gas saturation on sonochemiluminescence intensity resulting from microfluidic reactions. J Phys Chem A 117(41):10598–10603
85. Smart EJ, Ying Y-S, Mineo C, Anderson RG (1995) A detergent-free method for purifying caveolae membrane from tissue culture cells. Proc Natl Acad Sci 92(22):10104–10108
86. Hughes DE, Nyborg WL (1962) Cell disruption by ultrasound. Streaming and other activity around sonically induced bubbles is a cause of damage to living cells. Science 138 (3537):108–114
87. Schilling EA, Kamholz AE, Yager P (2002) Cell lysis and protein extraction in a microfluidic device with detection by a fluorogenic enzyme assay. Anal Chem 74(8):1798–1804
88. Waters LC, Jacobson SC, Kroutchinina N, Khandurina J, Foote RS, Ramsey JM (1998) Microchip device for cell lysis, multiplex PCR amplification, and electrophoretic sizing. Anal Chem 70(1):158–162
89. Wang H-Y, Bhunia AK, Chang L (2006) A microfluidic flow-through device for high throughput electrical lysis of bacterial cells based on continuous dc voltage. Biosens Bioelectron 22(5):582–588
90. Di Carlo D, Jeong K-H, Lee LP (2003) Reagentless mechanical cell lysis by nanoscale barbs in microchannels for sample preparation. Lab Chip 3(4):287–291

91. Boettner M, Prinz B, Holz C, Stahl U, Lang C (2002) High-throughput screening for expression of heterologous proteins in the yeast Pichia pastoris. J Biotechnol 99(1):51–62
92. Daly R, Hearn MTW (2005) Expression of heterologous proteins in Pichia pastoris: a useful experimental tool in protein engineering and production. J Mol Recognit 18(2):119–138
93. Marentis TC, Kusler B, Yaralioglu GG, Liu S, Hæggström EO, Khuri-Yakub BT (2005) Microfluidic sonicator for real-time disruption of eukaryotic cells and bacterial spores for DNA analysis. Ultrasound Med Biol 31(9):1265–1277
94. Nan L, Jiang Z, Wei X (2014) Emerging microfluidic devices for cell lysis: a review. Lab Chip 14(6):1060–1073
95. Augustsson P, Magnusson C, Nordin M, Lilja H, Laurell T (2012) Microfluidic, label-free enrichment of prostate cancer cells in blood based on acoustophoresis. Anal Chem 84 (18):7954–7962
96. Yang AHJ, Soh HT (2012) Acoustophoretic sorting of viable mammalian cells in a microfluidic device. Anal Chem 84(24):10756–10762
97. Ding X, Steven Lin S-C, Lapsley MI, Li S, Guo X, Chan CY, Chiang I-K, Wang L, McCoy JP, Huang TJ (2012) Standing surface acoustic wave (SSAW) based multichannel cell sorting. Lab Chip 12(21):4228–4231
98. Wang QX, Yeo KS, Khoo BC, Lam KY (1996) Strong interaction between a buoyancy bubble and a free surface. Theor Comput Fluid Dyn 8(1):73–88
99. Klaseboer E, Khoo BC (2004) An oscillating bubble near an elastic material. J Appl Phys 96 (10):5808–5818
100. Chin CD, Laksanasopin T, Cheung YK, Steinmiller D, Linder V, Parsa H, Wang J et al (2011) Microfluidics-based diagnostics of infectious diseases in the developing world. Nat Med 17 (8):1015–1019
101. Warner EA, Kotz KT, Ungaro RF, Abouhamze AS, Lopez MC, Cuenca AG, Kelly-Scumpia KM et al (2011) Microfluidics-based capture of human neutrophils for expression analysis in blood and bronchoalveolar lavage. Lab Invest 91(12):1787–1795
102. Kotz KT, Xiao W, Miller-Graziano C, Qian W-J, Russom A, Warner EA, Moldawer LL et al (2010) Clinical microfluidics for neutrophil genomics and proteomics. Nat Med 16 (9):1042–1047
103. Whitesides GM (2006) The origins and the future of microfluidics. Nature 442(7101):368–373